JOURNAL OF GEOPHYSICAL RESEARCH, VOL. 104, NO. B4, PAGES 7419–7441, APRIL 10, 1999

Kinematics of the Pacific-North America plate boundary zone, northern California

Jeffrey T. Freymueller,[1] Mark H. Murray,[2] Paul Segall, and David Castillo[3]
Department of Geophysics, Stanford University, Stanford, California

Abstract. We measured motions of 54 sites in an east-west transect across northern California at 38°-40° north by Global Positioning System (GPS) observations over a 4 year. We estimate the total slip rate on the San Andreas fault system to be $39.6^{+1.5}_{-0.6}$ mm/yr (68.6% upper and lower confidence intervals from a nonlinear inversion are indicated by superscripts and subscripts). Slip rates on the individual faults are determined less precisely due to the high correlations between the estimated parameters. Our best fitting model fits the fault-parallel velocities with a mean square error of 1.04 and the following estimated fault slip rates (all in mm/yr): San Andreas $17.4^{+2.5}_{-3.1}$, Ma'acama $13.9^{+4.1}_{-2.8}$, and Bartlett Springs $8.2^{+2.1}_{-1.9}$. The data are fit best by models in which the San Andreas fault is locked to $14.9^{+12.5}_{-7.1}$ km, the Ma'acama fault locked to $13.4^{+7.4}_{-4.8}$ km except for shallow creep in the upper 5 km, and the Bartlett Springs fault creeping at all depths. The Ma'acama fault most likely poses a significant seismic hazard, as it has a high slip rate and has accumulated a slip deficit large enough to generate a magnitude 7 earthquake. We find little evidence for contraction across Coast Ranges, except at western edge of Great Valley where 1-3 mm/yr of shortening is permitted by the data. No strain is observed within the Great Valley or Sierra Nevada except that associated with right-lateral strike slip on the San Andreas fault system. This is consistent with models of the Pacific–North America plate boundary zone in which the relative plate motion is partitioned into two domains, one strike-slip and one dominantly extensional, separated by the elastically deforming Sierra Nevada-Great Valley block.

1. Introduction

The ~100 km wide San Andreas fault system in northern California is composed of three subparallel right-lateral faults; from west to east, the San Andreas, Ma'acama, and Bartlett Springs faults (Figure 1). The latter two faults represent the northwestward extension of the Hayward and Calaveras faults in the San Francisco Bay area. This paper presents new geodetic measurements of the interseismic velocity field along the northern San Andreas fault system, which constrain fault slip rates and estimates of seismic hazard in northern California.

Although the San Andreas fault north of the San Francisco Bay area has been essentially aseismic since the great 1906 San Francisco earthquake, faults northeast of the San Andreas have been seismically active. Two prominent seismic zones corresponding to the traces of the Ma'acama and the Bartlett Springs Faults [*Hill et al.*, 1990] extend as far north as the surface projection of the subducting Gorda slab (Figure 1). Seismicity along the Ma'acama and the Bartlett Springs faults dips to the northeast 60° to 75°, and earthquake focal mechanisms exhibit right-lateral to oblique right-reverse faulting [*Castillo and Ellsworth*, 1993]. Seismic activity across the Great Valley and western Sierra Nevada is generally low. There is, however, a northwest trending seismic lineament between Lake Tahoe and Mount Shasta (Figure 1) that includes the magnitude 6 strike-slip 1966 Truckee earthquake.

Paleoseismic studies place strong constraints on the San Andreas slip rate and weaker constraints on the slip rates of the other faults. *Niemi and Hall* [1992] estimated the slip rate on the San Andreas at the Vedanta Retreat wind gap, near Point Reyes to be 23 ± 3 mm/yr. Farther north at Point Arena, where the fault goes offshore, *Prentice* [1989] estimated the slip rate to be 25 ± 3 mm/yr. The Ma'acama fault, situated about 45-50 km east of the San Andreas, is the northern member of the Hayward–Rodgers Creek–Healdsburg–Ma'acama fault system. Offset channels in alluvial fan deposits across the Rodgers Creek fault yield a minimum slip rate of 3.8 to 5.8 mm/yr during the past 1300 years [*Budding et al.*, 1991]. *Schwarz et al.* [1992] estimated a slip rate of 6.4 to 10.4 mm/yr for the Rodgers Creek fault. The Bartlett Springs fault, located 35-40 km east of the Ma'acama fault, is the northern member of the Calaveras–Green Valley–Bartlett Springs fault system. The Green Valley fault exhibits aseismic creep of 5 mm/yr based on offset cultural features between 1922 and 1974 [*Frizell and Brown*, 1976].

Fault strikes are roughly constant from the San Francisco Bay region north to about the latitude of Point Arena, at which point the strikes of all faults in the San Andreas system begin to rotate clockwise to a more northerly direction. Immediately north of Point Arena, the San Andreas fault bends 20° clockwise (a releasing bend) and continues with a more northerly trend [*Curray and Nason*, 1967]. About 125 km north of Point Arena, in the generally accepted interpretation (Figure 1), the San Andreas undergoes a significant counterclockwise (compressive) bend before cutting across

[1] Now at Geophysical Institute, University of Alaska, Fairbanks.
[2] Also at Seismological Laboratory, University of California, Berkeley.
[3] Now at Department of Geology and Geophysics, University of Adelaide, Australia.

Paper Number 1998JB900118.
0148-0227/99/1998JB900118$09.00.

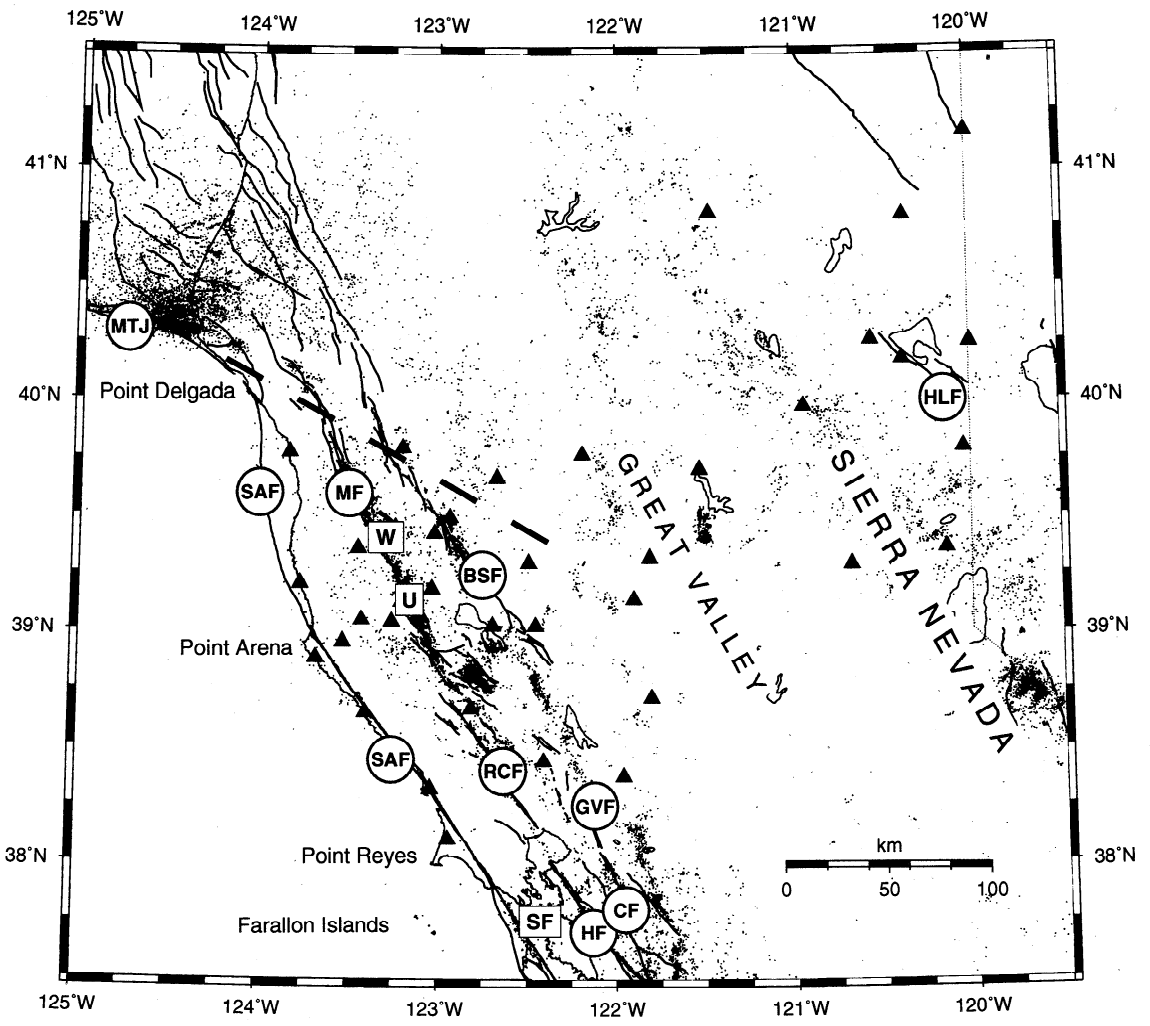

Figure 1. Location map showing the study area, mapped active faults, and a representative set of GPS sites. A dense cluster of GPS sites is located near Point Arena. Active faults referenced in this paper are labeled with circled initials, from south to north, HF Hayward fault; CF Calaveras fault; SAF, San Andreas fault; RCF, Rodgers Creek fault; GVF, Green Valley fault; BSF, Bartlett Springs fault; MF, Ma'acama fault; MTJ, Mendocino Triple Junction; HLF, Honey Lake fault. Cities and towns are labeled with initials inside boxes, from south to north, SF, San Francisco; U, Ukiah; W, Willits. Clear Lake is the lake located just south of the "BSF" label, and Lake Pillsbury is located just to the northwest of the same label. The south edge of the Gorda slab [*Jachens and Griscom*, 1983; *Furlong et al.*, 1989] is indicated by a heavy dashed line. Crustal seismicity is plotted based on the Berkeley catalog. All earthquakes are plotted for the time range 1967-1998, with magnitude >1.5 and recorded on at least 10 stations.

Point Delgada and continuing offshore to the Mendocino Triple Junction [*Curray and Nason*, 1967].

The motion of the Pacific plate relative to North America in northern California is 46 mm/yr N35°W according to the NUVEL-1A model [*DeMets et al.*, 1990, 1994]. While most of this motion is accommodated along the San Andreas fault system, it has long been recognized that Basin and Range extension contributes a significant component to the overall plate motion [e.g., *Minster and Jordan*, 1987; *Ward*, 1990]. It has been proposed that the Sierra Nevada and Great Valley (SNGV) make up a nondeforming block [*Wise*, 1963; *Wright*, 1976] bounded on the west by the San Andreas fault system, on the south by the Garlock fault, and on the southeast and east by the Eastern California Shear Zone and the Owens Valley Fault Zone. A component of the deformation associated with the Eastern California Shear Zone might possibly extend along the previously mentioned zone of seismicity trending northwest from Lake Tahoe, possibly into southern Oregon [*Pezzopane and Weldon*, 1993]. Very little is known, however, about the magnitude or sense of motion across this zone.

2. Previous Geodetic Results

Very long baseline interferometry (VLBI) measurements at four stations near the Sierra Nevada block (Hat Creek, Quincy, Mammoth, and Owens Valley) and three stations near the San Andreas fault (Point Reyes, Presidio, and Fort Ord) provide valuable constraints on the integrated deformation across northern California [e.g., Gordon et al., 1993; Ma et al., 1995]. The VLBI stations near the San Andreas move in the same direction, and at nearly the same rate, as predicted by the NUVEL-1A model for the Pacific–North America plate boundary. Remarkably, the Point Reyes station which is only

5 km west of the San Andreas, well within the zone of elastic strain accumulation, is moving at 91% of the NUVEL-1A predicted rate (42 mm/yr toward N37°W). Relative to the Pacific plate, Point Reyes moves only 7 mm/yr.

Hat Creek, Quincy, and Owens Valley have similar VLBI-derived velocities, about 11-13 mm/yr in a northwesterly direction relative to the North American plate. The velocities of the latter two sites have been used to infer the motion of an assumed rigid Sierra Nevada Great Valley (SNGV) block, making corrections for the motion of the Owens Valley station with respect to the Sierra Nevada using nearby terrestrial geodetic measurements [Argus and Gordon, 1991; Dixon et al., 1995]. The relative rotation pole inferred by Dixon et al. [1995] predicts 4 ± 2 mm/yr of San Andreas-normal convergence between the SNGV block and the Pacific plate. Argus and Gordon [1991] predict 2 ± 2 of fault-normal convergence. The relative rotation pole for the Sierra Nevada relative to the Pacific plate can be inferred from the Argus and Gordon [1991] Sierra Nevada–North America pole and the NUVEL-1A North America–Pacific pole; the resulting pole is (44.0°N, 103.8°W, 0.916°/Myr), with a clockwise rotation of the Sierra Nevada relative to the Pacific. A similar pole (46.0°N, 83.4°W, 1.033°/Myr) has been obtained from VLBI data alone (D. Argus, personal communication, 1997). The difference between these two poles, which will be referred to as SNGV-PCFC$_1$ and SNGV-PCFC$_2$ respectively, results from the difference between the NUVEL-1A and VLBI North America–Pacific poles. The rigid block model is of course an approximation, and any interpretation of geodetic data must account for elastic strain accumulation on faults bounding the putative SNGV block. There are far too few VLBI sites to determine how strain or slip is partitioned between the active faults of the San Andreas system.

More detailed spatial information on the distribution of deformation in northern California has come from repeated laser trilateration (Geodolite) measurements, summarized by *Lisowski et al.* [1991]. The cumulative fault-parallel displacement rate across the 115 km wide network at Point Reyes is 31 ± 3 mm/yr. Shear strain is concentrated in the immediate vicinity of the San Andreas fault, 0.64 ± 0.07 μrad/yr [*Prescott and Yu*, 1986], with a nearly constant velocity gradient extending northeast of the San Andreas. Strain rates of 0.1 μstrain/yr extend as far east as the western edge of the Great Valley, the eastern limit of the Geodolite network. Similar strain rates were determined from repeated triangulation measurements between 1931 and 1978 by *Cline et al.* [1985]. The velocity field inferred from Geodolite measurements is highly asymmetric about the San Andreas fault with nearly three-fourths of the observed motion northeast of the San Andreas. Only 1.5 ± 1.1 mm/yr of relative fault parallel motion occurs between Point Reyes Head and the Farallon islands (~15 and ~35 km west of the San Andreas Fault (SAF), respectively). *Williams et al.* [1994] find a similar distribution of motion across the north San Francisco Bay region based on Global Positioning System (GPS) surveys between 1990 and 1993. The GPS data, however, show insignificant deformation northeast of the Green Valley fault at the eastern end of the profile.

To the north, the Geodolite network narrows and is concentrated on The Geysers geothermal field south of Clear Lake. The network, which here is only 60 km wide, crosses the Rogers Creek–Healdsburg–Ma'acama fault zone, with only one station east of the Bartlett Springs–Green Valley fault zone. Geodolite data from 1974 to 1982 (M. Lisowski, personal communication, 1991) shows a net fault parallel velocity of ~20 mm/yr across this region. Note that this value excludes motion associated with the San Andreas fault west of the network. The data also suggest additional unmeasured deformation east of the network. There is a 50 km gap in the U.S. Geological Survey (USGS) trilateration network between The Geysers and the Covelo-Mendocino area. The Covelo network is ~45 km wide and spans small sections of the Ma'acama and Lake Mountain fault zones, near GPS site HPGN 0104. The net fault-parallel velocity from 4 years of Geodolite surveys is ~20 mm/yr, with roughly half of this occurring on the Ma'acama fault and the other half on the Lake Mountain fault (M. Lisowski, personal communication, 1991). In summary, the trilateration networks in all likelihood did not span the entire zone of active crustal deformation.

Prescott and Yu [1986] suggest several models to explain the asymmetric deformation concentrated east of the San Andreas fault. One model that fits the Geodolite observations involves 10 mm/yr of slip beneath the San Andreas, Ma'acama, and Bartlett Spring faults. An alternate model which fits the Geodolite data equally well, involves 30 mm/yr of continuously distributed slip at depth between the San Andreas and West Napa faults. Both models appear inconsistent with the geologic slip rate data summarized at the beginning of section 1. Furthermore, neither model explicitly considers viscous relaxation of the lower crust following past earthquakes on the San Andreas and other faults. *Prescott and Yu* [1986] note that, assuming slip in a uniform elastic half-space, the high local strain rate across the SAF implies a very shallow locking depth, of the order of 6 km near Point Reyes. 1906 displacements from Point Arena imply substantial slip beneath 6 km depth [*Matthews and Segall*, 1993]. These two observations may not be in conflict if the locking depth or elastic properties of the SAF vary along strike.

Lisowski et al. [1991] note that differing elastic properties on either side of the San Andreas may help explain the steep velocity gradient and pronounced asymmetry across the fault. A low modulus shear zone centered on the fault also concentrates strain above the fault zone. *Li and Rice* [1987] consider models with a lower crustal viscoelastic channel, and *Fares and Rice* [1989] suggest that the absence of a lower crustal viscoelastic channel on the more mafic Pacific plate could explain the asymmetric pattern of deformation across the San Andreas. These models, however, include only a single strike-slip fault (the San Andreas) and do not account for known deformation associated with the Ma'acama and Bartlett Spring faults.

Despite numerous investigations, a number of outstanding questions remain. How is slip partitioned between the faults of the San Andreas fault system? Does the pronounced asymmetry in deformation across the San Andreas observed at Point Reyes characterize the entire plate boundary between the San Francisco Bay and the Mendocino triple junction? Is the concentrated strain at the San Andreas a general feature north of the latitude of Point Reyes? How far east does measurable deformation associated with the SAF system extend? Is there detectable shear associated with the hypothesized northern extension of the eastern California shear zone along the western margin of the Basin and Range province?

In this paper we begin to address these questions with GPS measurements at about 50 sites in northern California,

Table 1. Measurement Campaigns

Date	Type	Region(s) Covered
	Major Campaigns	
July 1991	global	Point Arena, partial Coast Ranges
June-Aug. 1991	global	Caltrans HPGN
Sept. 1991	global	partial Coast Ranges
July 1992	global	Point Arena
Sept. 1992	global	Coast Ranges, Sierra Nevada
Sept. 1993	global	Coast Ranges
July 1994	global	Coast Ranges, Sierra Nevada, partial Point Arena
Sept. 1995	regional	Coast Ranges
	Minor Campaigns	
May 1992	global	Caltrans Mendocino postearthquake
Jan.-Feb. 1993	regional	Caltrans Coast Ranges
May 1993	regional	Caltrans Coast Ranges
June 1993	regional	Caltrans North Bay
July-Sept. 1993	regional	Caltrans central California
Nov. 1993	global	Caltrans Coast Ranges
Jan. 1994	global	Caltrans Coast Ranges
Feb.-Mar. 1994	global	NGS HPGN reoccupation
April 1994	global	NGS HPGN reoccupation
July 1994	global	Caltrans West Bay
Sept. 1994	global	partial Coast Ranges

The global solution type indicates loosely constrained solutions were generated, with orbits estimated based on a global distribution of sites estimated along with the Northern California sites. The regional solution type indicates that orbits from the International GPS Service (IGS) or the Jet Propulsion Laboratory (JPL) IGS submission were fixed and a regional (North American) set of sites were analyzed along with the Northern California sites. In general, only a few sites from these regional solutions were used in the velocity solution. See the Data Analysis section for details. HPGN, High Precision Geodetic Network; Caltrans, California Department of Transportation; NGS, National Geodetic Survey.

stretching from the Pacific coast to the westernmost Basin and Range collected between 1991 and 1995 (Figure 1).

3. Measurements and Analysis

3.1. Field Measurements

3.1.1. Campaigns. The majority of the data used in this study come from GPS field campaigns undertaken by Stanford University personnel between 1991 and 1995 (Table 1). There were two separate major field campaigns in 1991 and 1992, each covering different parts of the network, and yearly major campaigns from 1993 to 1995. In addition to the major campaigns, important data were collected during 11 minor campaigns. Minor campaigns are those in which only a small amount of data were collected, or in which only a small fraction of the data collected are used in this study. Most of the minor field campaigns were carried out by other agencies such as the California Department of Transportation (Caltrans) and the National Geodetic Survey (NGS); in some of these minor campaigns simultaneous measurements were made by Stanford. Other minor campaigns are surveys carried out mainly to tie together multiple survey markers at a single site. The minor campaigns are critical for the velocity determinations of a few sites, but for the sites surveyed most often they are not important. We also include data from permanent sites in and around northern California. The number of permanent sites in northern California increased from two with poor data quality in 1991 to 11 high-quality sites in 1995.

During each major field campaign, we surveyed one or more subsets of the complete network. These subsets are useful for descriptive purposes: Point Arena, a cluster of sites with past Geodolite measurements across the San Andreas fault near Point Arena; Coast Ranges, the main network in the Coast Ranges and western Great Valley; and Sierra Nevada, a subset of the statewide California High Precision Geodetic Network (HPGN) network in the Sierra Nevada between Lake Tahoe and Mount Lassen. In general, whenever we surveyed a subset of the network, we surveyed the complete subset. The main Coast Ranges sites were surveyed at least once a year (Table 1), and their velocities are correspondingly more precise than the other sites.

The July 1991 field campaign was carried out in conjunction with the HPGN survey. The Sierra Nevada subset, surveyed in 1992 and 1994, is made up entirely of HPGN sites, and the sites we used in the Central Valley are also part of the HPGN network. During the September 1995 campaign, measurements were made for the first time at a number of sites surveyed in separate efforts by the U.S. Geological Survey, the beginning of an effort to link together all geodetic networks in northern California into a consistent kinematic frame.

All 1991 surveys, including the HPGN survey, and the July 1992 survey used a minimum of two occupations, each of 6 hours duration, on separate days. Beginning in September 1992, we increased the scheduled occupation time for all of our sites from 6 to 8 hours each day (still with at least two occupations on separate days), and we began to observe for 24-hour sessions at secure sites. In addition, we increased the efficiency of our surveys by using the same receiver at one site during the daylight hours (8-hour session) and at a second site unattended at night (14-hour session). Because of improvements in field observation strategy and the completion of the GPS constellation, results for September 1992-1995 are significantly more precise, by about a factor of 2, than the 1991 to July 1992 results. A small improvement in the precision of the most recent surveys can be attributed to an equipment upgrade from Trimble SST to SSE receivers.

3.1.2. Sites. Data from more than 70 sites were used over the course of the project, of which 11 are regional permanent sites (Table 2); precise velocities for 54 sites are presented in this paper. The remaining sites are either outside of the main field area or lack enough data to determine a precise velocity. Multiple survey marks were used at four sites. Multiple markers were used at the sites Boyle and Clark 2 because we wished to compare the GPS results to Geodolite data, which used multiple nearby marks due to line of sight restrictions. At the site View we used three separate marks because the original was destroyed between the 1993 and 1994 surveys. In 1994 a plastic survey marker was found near the original mark. A new marker was set in 1995 and was surveyed along with the plastic marker. At the site Prather, there were two survey markers about 4 m apart, and we used both marks because the first two occupations of the site were made by different survey personnel who occupied different markers.

3.1.3. Equipment Used. Stanford University field data were collected using Trimble 4000 series receivers, the 4000 SST (SST) and 4000 SSE (SSE). The SST receiver is an L2-squaring receiver that records dual-frequency phase measurements (half wavelength on L2) and C/A code range measurements, while the SSE is a code-correlating receiver that records full wavelength dual frequency phase and range measurements. Prior to September 1993, all of our field data

Table 2. Sites observed during this project

Site	ID	Latitude	Longitude	Monument Stamping	Monument Type	Agency	Observed
Biaggi	BIAG	39° 57.83	-123° 40.00	BIAGGI 1977	rod driven to refusal	NCER	91, 92
Boyle	BOYL	39° 58.93	-123° 42.25	BOYLE 1929	disk in concrete	USC&GS	91, 92, 94
Cable+	CBLE	39° 58.93	-123° 42.25	(unstamped)	bent nail in concrete	-----	92
Chert	CHER	39° 02.50	-123° 15.00	CHERT 1991	disk in rock outcrop	Stanford	91, 92, 93, 94, 95
Clark 2	CLAR	38° 59.50	-123° 38.00	CLARK 2 1930	disk in concrete	USC&GS	92, 93, 94, 95
Clark Eccentric+	CECC	38° 59.50	-123° 38.00	CLARK ECC 1983	rod driven to refusal	NCER	91, 92
Gonzo+	GONZ	38° 59.50	-123° 38.00	GONZO 1983	rod driven to refusal	NCER	91, 92
Cold Springs	COLD	39° 01.00	-123° 31.17	COLD SPRINGS 1938	disk in rock outcrop	US Forest	91, 92, 93, 94, 95
Cord	CORD	38° 11.15	-122° 35.71	CORD	pin in rock outcrop	USGS	94, 95
Dunn	DUNN	39° 00.75	-123° 38.75	DUNN 1891 1919	disk in concrete	USC&GS	91, 92, 94
Farallon	FARB	37° 41.83	-123° 00.04	(unstamped)	(permanent)	UCB	94+ perm.
Fire	FIRE	39° 12.63	-123° 10.02	FIRE 1991	rod driven to refusal	Stanford	91, 92, 93, 94, 95
Hat Creek	HATC	40° 49.07	-121° 28.28	HAT CREEK NCMN D 1985	disk in rock outcrop	NASA	90, 91, 92, 94
High Bluff	HBLF	38° 54.00	-123° 41.75	HIGH BLUFF 1879 1929	disk in concrete	USC&GS	91, 92, 94, 95
Hogs	HOGS	39° 27.50	-123° 13.50	XX 959 1963	disk in rock outcrop	USC&GS	91, 92, 93, 94, 95
HPGN 0101	0101	39° 01.68	-122° 27.12	HPGN-CALIF. STA 01-01 1991	rod driven to refusal	Caltrans	91, 92, 93, 94, 95
HPGN 0102	0102	39° 11.18	-123° 01.97	HPGN-CALIF. STA 01-02 1991	rod driven to refusal	Caltrans	91, 92, 93, 94, 95
HPGN 0103	0103	39° 12.67	-123° 45.93	HPGN-CALIF. STA 01-03 1991	rod driven to refusal	Caltrans	91, 92, 93, 94, 95
HPGN 0104	0104	39° 47.75	-123° 11.98	HPGN-CALIF. STA 01-04 1991	rod driven to refusal	Caltrans	91, 92, 93, 94, 95
HPGN 0105	0105	39° 46.63	-123° 50.03	HPGN-CALIF. STA 01-05 1991	rod driven to refusal	Caltrans	91, 92, 93, 94, 95
HPGN 0106	0106	40° 27.61	-123° 31.41	HPGN-CALIF. STA 01-06 1991	rod driven to refusal	Caltrans	91, 92, 94
HPGN 0108	0108	40° 48.92	-123° 29.61	HPGN-CALIF. STA 01-08 1991	rod driven to refusal	Caltrans	91, 92, 94
HPGN 0109	0109	40° 58.50	-124° 07.04	HPGN-CALIF. STA 01-09 1991	rod driven to refusal	Caltrans	91, 92, 94
HPGN 0114	0114	38° 53.45	-123° 40.75	HPGN-CALIF. STA 01-14 1991	rod driven to refusal	Caltrans	91, 94
HPGN 01EE	01EE	39° 21.26	-123° 36.86	CA-HPGN-D STA 01-EE 1993	rod driven to refusal	Caltrans	94, 95
HPGN 0220	0220	40° 47.95	-120° 21.98	HPGN 0220 1991	rod driven to refusal	Caltrans	91, 92, 94
HPGN 0226	0226	40° 14.69	-119° 59.66	HPGN 0226 1991	rod driven to refusal	Caltrans	91, 94
HPGN 0301	0301	39° 40.50	-122° 42.50	HPGN 0301 1991	rod driven to refusal	Caltrans	91, 92, 93, 94, 95
HPGN 0303	0303	39° 42.28	-121° 31.83	HPGN 0303 1991	rod driven to refusal	Caltrans	91, 92, 94
HPGN 0306	0306	39° 17.60	-120° 40.79	HPGN 0306 1991	rod driven to refusal	Caltrans	91, 92, 94
HPGN 0411	0411	38° 19.44	-123° 02.29	HPGN 0411 1990	rod driven to refusal	Caltrans	91, 93, 94
HPGN 0412	0412	38° 26.47	-122° 24.41	HPGN 0412 1990	rod driven to refusal	Caltrans	91, 93, 94
HPGN 0413	0413	38° 39.25	-123° 24.00	HPGN 0413 1990	rod driven to refusal	Caltrans	91, 92, 93, 94, 95
HPGN 0414	0414	38° 40.25	-122° 48.67	HPGN 0414 1990	rod driven to refusal	Caltrans	91, 92, 93, 94, 95
Kneeland	KNEE	40° 43.60	-123° 58.49	KNEELAND 1932 TTNO-Y-1932	disk in rock outcrop	USC&GS	91, 92, 94
KOA	KOA	39° 24.50	-123° 23.00	KOA 1991	disk in rock outcrop	Stanford	91, 92, 93, 94, 95
Lane	LANE	39° 00.75	-123° 41.50	LANE 1891 1919	disk in concrete	USC&GS	91, 92, 94
Lodoga	LODO	39° 18.07	-122° 29.50	LODOGA 1949	disk in concrete	USC&GS	91, 93, 94, 95
Orland	ORLA	39° 46.12	-122° 11.53	ORLAND S. BASE 1939	disk in concrete	USC&GS	91, 92, 94, 95
OZB	OZB	38° 57.25	-123° 39.75	OZB 1991	rod driven to refusal	Stanford	91, 92
OZ+	OZ	38° 57.25	-123° 39.75	OZ 1977	rod driven to refusal	NCER	92
Piper	PIPE	38° 57.50	-123° 35.00	PIPER 1991	disk in rock outcrop	Stanford	91, 92, 93, 94, 95
Point Reyes	PTRY	38° 06.22	-122° 56.18	POINT REYES NCMN 1981	disk in concrete	NGS	91, 92, 93, 94, 95
Polaris	POLA	39° 21.47	-120° 08.52	POLARIS 1979	disk in concrete	Caltrans	91, 92, 94
Prather	PRAT	39° 03.00	-123° 25.25	PRATHER 2	rod driven to refusal	Stanford	91, 92, 93, 94
Prather Caltrans*	PRTC	39° 03.00	-123° 25.25	PRATHER 3-72	disk in concrete	Caltrans	91, 94
Presidio	PRES	37° 48.31	-122° 27.30	JPL-MV 1981	disk in concrete pad	NASA	91, 93, 94, 95
Point Arena	PTAR	38° 55.25	-123° 43.50	PT ARENA LAT STA 1870 1929	disk in concrete	USC&GS	91, 92, 93, 94, 95
Quincy	QUIN	39° 58.47	-120° 56.65	7221 1982	disk in concrete pad	NASA	92+ perm.
Red Mountain	RED	39° 05.92	-123° 05.40	RED USGS 1949 1976	disk in concrete	USGS	91, 92, 93, 94, 95
Rey	REY	39° 27.50	-123° 20.50	REY 1991	disk in rock outcrop	Stanford	91, 92, 93, 94, 95
Rickard	RICK	38° 58.00	-123° 39.25	RICKARD 1977	rod driven to refusal	NCER	91, 92
Sage	SAGE	39° 47.45	-120° 02.32	SAGE 1966	disk in concrete	Caltrans	91, 92, 94
Schuller	SCHU	39° 57.75	-123° 39.17	SCHULLER 1977	rod driven to refusal	NCER	91, 92
Shoemaker 2	SHOE	38° 58.00	-123° 41.00	(unstamped)	screw in concrete+	USC&GS	92
Slide	SLID	39° 25.50	-123° 01.25	SLIDE 1991	disk in rock outcrop	Stanford	91, 92, 93, 94, 95
Spur 2 RM5	SPUR	38° 54.00	-123° 40.50	SPUR 2 RM5	disk in concrete	USC&GS	91, 92
Thompson	THOM	40° 15.68	-120° 33.48	THOMPSON 1931	disk in rock	USC&GS	91, 92
Two Rock	2ROC	39° 22.00	-123° 27.00	TWO ROCK 1879 1925	disk in rock outcrop	USC&GS	91, 92, 93, 94, 95
Ukiah Airport	UKIA	39° 07.97	-123° 12.17	UKIAH AIRPORT 1949 1965	disk in concrete	USC&GS	91, 92, 93, 94, 95
Vacaville RM5	VAC5	38° 22.48	-121° 57.48	VACAVILLE NCMN NO 5 1983	disk in concrete	NGS	91, 94, 95
View	VIEW	39° 29.13	-122° 52.07	VIEW 1991	disk in rock outcrop	Stanford	91, 92, 93
View*	FHWA	39° 29.13	-122° 52.07	FHWA	plastic cap in rock	Fed. Hwy.	94, 95
View*	NOV1	39° 29.13	-122° 52.07	NO VIEW	disk in rock outcrop	Stanford	95

Only those sites used in this paper are listed. Agency indicates the organization that established the site, or in the case of permanent sites the agency that operates the site. Caltrans, California Department of Transportation; Fed. Hwy., Federal Highway Administration; NASA, National Aeronautic and Space Administration; NCER, National Center for Earthquake Research; NGS, National Geodetic Survey; Stanford, Stanford University; UCB, University of California, Berkeley; USC&GS, U. S. Coast and Geodetic Survey; USGS, U. S. Geological Survey.

* Secondary marks. These are listed immediately after their main mark.

+ Screw replaces disk that was pried out prior to all GPS or EDM measurements.

were collected using SST receivers. The September 1993 major campaign included a mixture of SST and SSE receivers, and the 1994 and 1995 major campaign used SSE receivers exclusively. Most data from Caltrans and NGS were collected using Trimble receivers as well, with an upgrade from SST to SSE in 1993. Ashtech MD-XII receivers, L2-squaring receivers like the SST, were used at some HPGN sites during the 1991 HPGN survey and at the two oldest regional permanent sites, Chabot and Winton. Ashtech P-XII and Z-XII receivers were used at the other permanent sites, except for Quincy which uses a TurboRogue SNR-8000. These other receiver types are code-correlating receivers similar to the SSE, although all have internal differences that give them unique characteristics.

Several different antenna types were used over the course of this project. While the changes in receiver type result only in minor changes in data analysis procedures and have little impact on the solutions (other than the fact that solutions obtained with newer equipment are more precise), changes in antennas can directly impact accuracy through differences in antenna phase centers. The antenna used for the majority of the data is the Trimble Geodetic (SST) antenna. Except for a few sites occupied with Ashtech L1/L2 antennas during the HPGN survey, this antenna was used exclusively at all field sites until 1994. In the 1994 and 1995 campaigns, about 1/3 of the data were collected with the newer Trimble Compact (SSE) antenna. Including the Ashtech antennas used in the original HPGN survey and at the UC Berkeley and USGS permanent sites and the Dorne-Margolin antenna used at the Quincy permanent site, six different antenna types are found in our data set, making adequate modeling of phase center differences critical.

3.2. *Data Analysis*

Raw GPS data collected in the field were analyzed in 24-hour daily solutions together with data from regional and global permanent sites; a total of 168 days of GPS data were analyzed. We analyzed all data presented in this paper using the GIPSY/OASIS II software (release 4) developed at the Jet Propulsion Laboratory [*Zumberge et al.*, 1997; *Gregorius*, 1996]. The analysis methods used are described in more detail by *Larson et al.* [1997], except that we use an improved phase center model. We applied the IGS_01 phase center model, which is an average of several reliable determinations of antenna phase center mean locations and variation with elevation (M. Rothacher and G. Mader, 1996; ftp://igscb.jpl.nasa.gov/igscb/station/general/igs_01.pcv). Based on an antenna swap test carried out over a ~400 km baseline in Alaska, the error in relative coordinates after applying the IGS_01 model is of the order of 1 mm or less in the horizontal and 5 mm or less in the vertical for the Trimble Compact (SSE) and Dorne-Margolin with choke ring antennas (http://www.aeic.alaska.edu/Input/jeff/LBswap/LBswap_data.html). The long baseline swap test should give a reliable estimate of the magnitude of error from antenna mixing that would be expected in a regional network. Errors of this magnitude are comparable to the precision of 24 hour GPS sessions. We have not made a similar evaluation of the quality of the model for Ashtech antennas; however, the results should be similar because the same techniques were used in deriving all of the phase center models.

Carrier phase ambiguities were not resolved to integer values owing to poor algorithm performance with L2-squaring receivers on baselines longer than 30-50 km. Ambiguity resolution is most critical for the earliest surveys, which used the shortest occupations. However, since these surveys used L2-squaring receivers, ambiguity resolution did not consistently improve the actual precision as measured by day to day repeatability of solutions. Comparison of solutions with and without ambiguity resolution shows that some ambiguities were resolved to incorrect integer values, most likely due to incorrect determination of the widelane ambiguities, which in the absence of pseudorange measurements must be determined using assumptions about the differential ionospheric delay. As a result, the ambiguity-resolved solutions were no more precise on average than the ambiguity-free solutions.

In spite of our effort to use the best available model for antenna phase center variations, some significant antenna effects may remain unmodeled, especially the effect of scattering associated with the pillar mounts used at many permanent sites [*Elósegui et al.*, 1995]. For example, a change of antenna and antenna height at such a pillar at site PENT (Penticton, British Columbia, Canada) in February 1994 correlates with a step in the vertical coordinate of PENT of about 5 cm. Similar vertical offsets associated with changes of antenna height and the installation of conducting skirts at this type of marker have been noted (H. Dragert, personal communication, 1997). Similar effects have been seen in tripod setups only where the antenna is very close to the ground (J. Johnson, personal communication, 1995), so these kinds of errors are unlikely to bias coordinates at field sites. On the other hand, centering errors and blunders in measuring antenna heights can bias measurements at field sites but are less likely to affect measurements at permanent sites.

3.2.1. Orbits and Reference Frame. Two types of solutions were used in this study, global solutions with orbits estimated using a global network of tracking stations, and regional solutions using orbits fixed to values provided by Jet Propulsion Laboratory (JPL) International GPS Service (IGS) orbit submission. The two types of solutions are described in more detail below. All of the solutions were transformed into the ITRF94 reference frame (International Terrestrial Reference Frame 1994) [*Boucher et al.*, 1996]. We have found that relative coordinates (baselines) within our northern California network (spanning 150 km by 350 km) are not sensitive to the type of solution used, although the absolute coordinates of the sites are. The position of the northern California sites relative to permanent sites in western North America is sensitive to the type of solution used. We generated global orbit solutions whenever possible because the fixed orbit solutions show less consistency over time than our global solutions. This should be no surprise, since most of our data were taken before the official beginning of the IGS as an operational service, and there have been significant changes over time in models, processing strategies and reference frames used in producing the IGS orbits. In contrast, all of our global solutions use the latest models, the same reference frame, and the same means of realizing the reference frame. In order to minimize the inconsistencies inherent in using the two different types of solutions, we exclude sites outside of northern California from our velocity solutions.

Solutions using data from a global tracking network and the regional network are optimal since all relevant data are analyzed simultaneously. However, such solutions require much more time and effort than solutions using only the regional network and fixed orbits determined separately. When

is the extra time and effort worth it? At the beginning of this project, precise orbits were not generally available, so estimating orbits using a global solution was the only way to obtain the highest precision solutions. During the early period of the IGS, 1992 and 1993, precise orbits were available but the reference frame control was not satisfactory since different IGS centers fixed different stations, and the overall level of consistency was significantly lower than at present. We used fixed-orbit regional solutions from this time period only when a small number of stations in a small region were observed, so that inconsistencies in the reference frame would not contribute significant errors. The introduction of anti-spoofing in 1994 temporarily lowered the quality of the JPL IGS orbit submission, so we chose to analyze global solutions for the 1994 campaigns as well. By the time of the 1995 campaign, however, the benefit obtained by analyzing a global solution did not appear to be worth the effort, so we used fixed JPL orbits for these data.

3.2.1.1. Global Orbit Solutions: For the majority of data, global GPS solutions were estimated using all data from Northern California and western North America, along with a well-distributed set of global sites. The exact distribution of global sites varied with time as the global GPS network, now known as the IGS network, grew. Prior to 1993, all global sites were included in the solutions. Beginning in 1993, there were too many global permanent sites to use all of them as well as the field sites in the solutions, so some sites in dense regional clusters in southern California and western Europe were excluded. GPS satellite orbit parameters were estimated using the same models used by JPL in its current IGS analysis [*Zumberge et al.*, 1997]. For more detail, refer to *Larson et al.* [1997]. Instead of fixing or tightly constraining the coordinates of a set of sites in order to define a reference frame, we applied no significant coordinate constraints to our solutions. The resulting loosely constrained solutions can then be transformed into any desired reference frame. We transformed each daily loosely constrained solution into the ITRF94 reference frame by estimating the seven-parameter transformation that minimizes the misfit based on a set of globally distributed sites [*Heflin et al.*, 1992]. All of the major campaigns, with the exception of the 1995 campaign, were analyzed in this manner.

3.2.1.2. Regional Solutions: In the other type of solution, we analyzed the northern California data and a regional set of permanent sites covering western North America using fixed orbits obtained from JPL's submission to the IGS. Inclusion of the tracking stations improves estimation of satellite clock parameters and results in a more stable realization of the reference frame. Except for the treatment of the orbits and the number of sites used, these solutions are identical to the global orbit solutions described in section 3.2.1.1. The majority of these solutions date from 1993 and are in the ITRF91 reference frame. All regional solutions were transformed into ITRF94 using a series of transformation parameters derived by J. Kouba (personal communication, 1997). Relative coordinates within our network (~150 by 350 km) are changed at only the submillimeter level by the series of transformations. The practical realization of the reference frame in our regional solutions differs from that in our global solutions in that JPL fixed the coordinates of a different set of sites from those we used to define the transformation into the ITRF94 frame. Absolute coordinates in regional solutions can be biased by as much as 5-10 cm compared to an equivalent global orbit solution, although relative coordinates differ by <1 mm for pairs of sites within our northern California network.

3.2.2. Precision. Figure 2 shows the time evolution of the three baselines of varying lengths over 1991-1995, a long (1166 km) baseline between the permanent site at Penticton and Ukiah Airport (Figure 2a), a medium-length (117 km) regional baseline between Point Reyes and Ukiah (Figure 2b), and a short (11 km) baseline between Point Arena and Clark 2 (Figure 2c). Summary statistics for these three baselines and the permanent site baseline between Penticton and Quincy are given in Table 3. The weighted rms scatter about the best fit line for horizontal baseline components increase with baseline length from 2 mm for short baselines to 7-9 mm for long baselines. Typical minimum station separations within our network range from 10 to 50 km, and the entire northern California network spans about 150 by 350 km, so the two shorter baselines are most typical of those within the network. Penticton is the closest permanent site that was in operation for the entire time spanned by our campaigns, not counting sites in southern California that were displaced by earthquakes in 1992 and 1994. Penticton is also the closest permanent site with a velocity consistent with the stable North American plate [*Larson et al.*, 1997].

The large scatter in the 1991 estimates of the long baseline between Penticton and Ukiah result from the limited global tracking network available at that time. For comparison, the scatter for the baseline between Penticton and Quincy is notably smaller than that between Penticton and Ukiah even though the station separations are similar. There are no Quincy data from 1991 when the sparse global tracking network made reference frame definition more difficult. In addition, because Quincy and Penticton are both permanent sites, each daily observation of this baseline is always based on a 24-hour session, while the observing sessions at Ukiah vary from 8 to 24 hours, with less than half of the sessions at Ukiah being 24 hours in length. Finally, setup errors or antenna changes at Ukiah might increase the scatter of the baseline between Penticton and Ukiah, but very few changes were made to the permanent sites Penticton and Quincy.

3.2.3. Velocity Estimation. The individual daily GPS solutions were combined together to determine site velocities. Site positions at epoch 1993.0 and site velocities were estimated by standard weighted least squares techniques using the coordinates in the ITRF94 reference frame from the daily GPS solutions, weighted by the covariance matrix of the coordinates. The input covariances were scaled by a factor of 6.2, so that the reduced chi-square statistic of the velocity fit was equal to 1.0. A total of 168 daily GPS solutions spanning July 1991 to September 1995 were used to estimate velocities for 65 sites in northern California and three sites in western North America. Velocities are given relative to the Pacific plate (see below) in Table 4. We eliminated 1991 data for four sites in the northwestern part of the study area (HPGN 0104, HPGN 0105, Kneeland, and HPGN 0109) that were displaced by the 1992 Cape Mendocino earthquake [*Oppenheimer et al.*, 1993; *Murray et al.*, 1996].

During the HPGN survey, and to a lesser extent all of the surveys prior to the September 1992 establishment of the Quincy permanent site, the northern California network was isolated, located a considerable distance from the nearest permanent site (750 km to Goldstone, 1100 km to Penticton). During all of the early surveys carried out by Stanford we

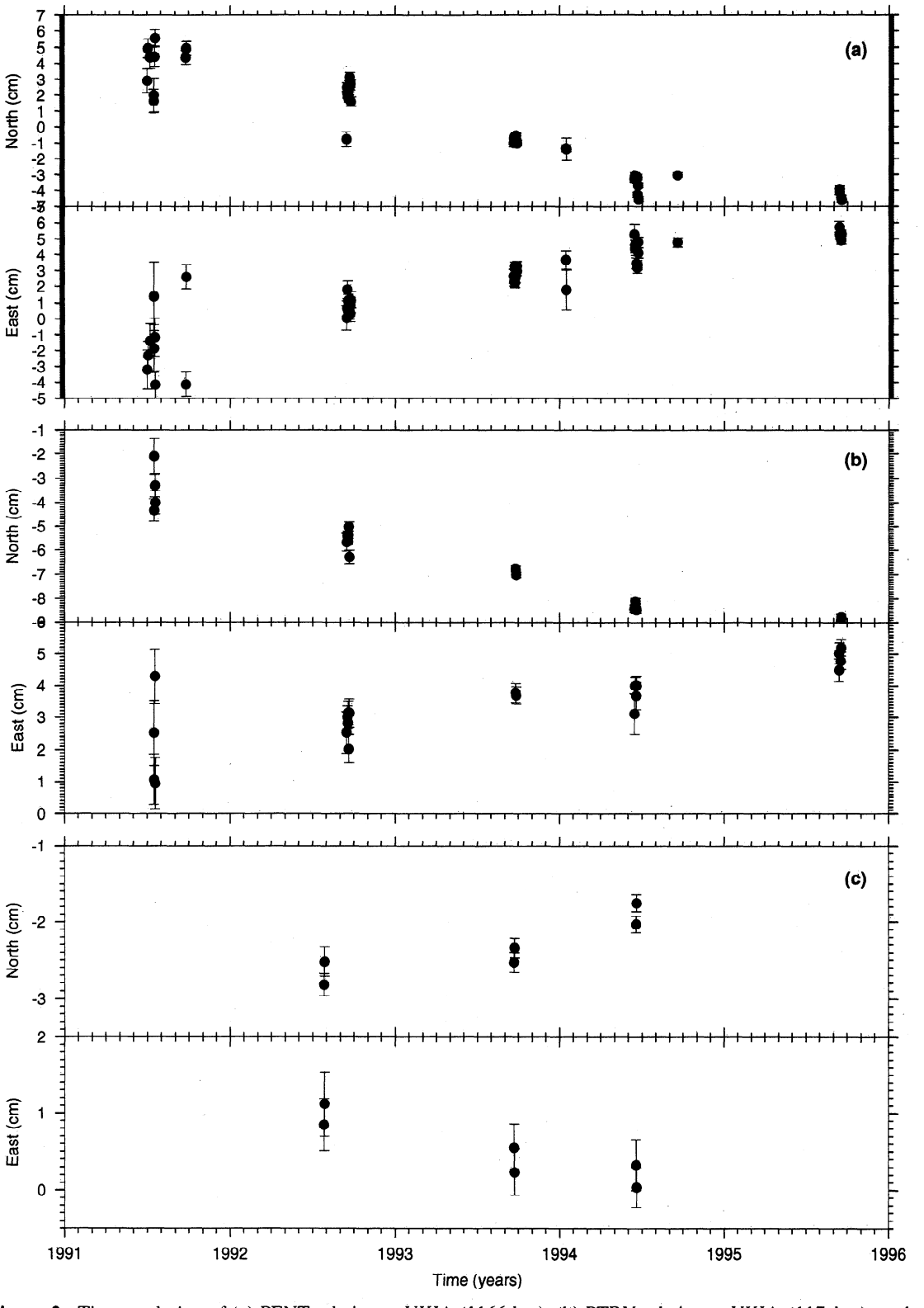

Figure 2. Time evolution of (a) PENT relative to UKIA (1166 km), (b) PTRY relative to UKIA (117 km), and (c) CLAR relative to PTAR (11 km) over 1991-1995 (see Table 3 for summary statistics). The improvement in precision over time is easily visible. Vertical scales are different for each baseline.

occupied at least one of the sites Point Reyes, Point Arena, or Ukiah every day. However, during some days of the HPGN survey only one or two of the sites in our main study area were occupied. In a case like this, we improve the velocity solution by including data from nearby sites that also have repeat measurements over time, although we do not report velocities for these other sites.

The precision of the estimated site velocities varies considerably from site to site. Three main factors affect the velocity precision of a given site. First, the number of site

Table 3. Summary Statistics for Sample Baselines

Baseline	Dist.	Days	East	North	Vert.
Penticton–Ukiah	1166	46	7	9	17
Penticton–Quincy	1043	100	5	5	19
Point Reyes–Ukiah	117	22	4	5	10
Point Arena–Clark	11	6	2	2	3

East, north and vert. give the weighted rms scatter in mm about the best fit line for each baseline component. Dist. gives the distance between the sites in km. Days gives the number of occupations of this baseline in the period 1991-1995. The best fit line and scatter are computed based only on data from the baseline in question and may be slightly different from the overall network velocity solution and misfit.

occupations varies from site to site. Second, while most of the sites were observed over the full period 1991-1995, some were measured over shorter periods. Finally, each site occupation varied from 8 hours to 24 hours, depending on the security at the site. The best determined sites, Point Arena and Ukiah, have a precision of about 0.6 mm/yr in the north component and 1.3 mm/yr in the east component relative to Point Reyes. The higher uncertainty in the east component results from not resolving phase ambiguities to their integer values. Velocities for most of the other main sites observed from 1991 to 1995 range from 1 to 1.5 mm/yr in the north component and 2 to 3 mm/yr in the east component. Vertical velocities have a precision ranging from 3 to 10 mm/yr, depending on site. Only three sites in the study area have vertical velocities more than 2σ away from zero: Hat Creek (+16 ± 6 mm/yr), Lane (+18 ± 7 mm/yr), and Thompson Peak (+16 ± 6 mm/yr). Since the best determined sites have velocities within 2σ of zero, and many within 1σ of zero, we will not consider the vertical velocities further. Note that one would expect random errors to cause three out of 60 sites to have apparent velocities exceeding two standard deviations, even if there were no actual vertical motion.

Velocities relative to Point Reyes, a well-measured site that was measured in the past using mobile Very Long Baseline Interferometry (VLBI), are shown for sites spanning the Coast Ranges of northern California (Figure 3). Without prior knowledge of the locations of the major faults within the Coast Ranges, it would be difficult to locate them using only the velocity field. The fault-parallel velocities vary smoothly from the Pacific coast to the western edge of the Great Valley, then are roughly constant over the western portion of the Great Valley. Four of the five sites east of the Bartlett Springs fault (Orland, HPGN 0101, HPGN 0301, View, and Lodoga) move with similar fault-parallel velocities, 31, 31, 28, 36, and 29 mm/yr relative to Point Reyes NCMN (all ± 2-3 mm/yr). The velocity of HPGN 0104, farther to the north, is somewhat smaller (26 ± 3 mm/yr).

We would like to express the velocities in a plate framework, as velocities relative to the Pacific plate. All of the sites on the Pacific plate are less than 10 km from the San Andreas fault, well within the zone of elastic deformation expected from a locked San Andreas fault. However, we can estimate the velocity of Point Reyes NCMN with respect to the stable interior of the Pacific plate based on two independent sources. *Ma et al.* [1995] estimated the velocity of Point Reyes NCMN relative to the Pacific plate to be 7 ± 1 mm/yr (fault-parallel), based on 7 years of mobile VLBI observations. *Williams et al.* [1994] presented velocities based on a 100-km-long GPS profile passing through Point Reyes and including Point Reyes NCMN and Point Reyes Head. They measured 6.2 ± 2 mm/yr of right-lateral motion between Point Reyes Head and Point Reyes NCMN. Adding the 1.5 mm/yr observed between Farallon and Point Reyes Head in the EDM-derived velocity field of *Lisowski et al.* [1991] gives 7.7 ± 2.5 mm/yr between the Farallons and Point Reyes NCMN. This is consistent with the VLBI estimate assuming that Farallon moves at stable Pacific plate velocity. Given the uncertainty in the NUVEL-1A Pacific–North America velocity, about 1.5 mm/yr, we use the VLBI estimate and adopt a velocity of 7 ± 2 mm/yr for Point Reyes NCMN relative to the Pacific plate. With this result we can estimate the velocities of all of the northern California sites relative to the Pacific plate. The velocity field is highly asymmetric about the San Andreas fault, with almost all sites west of the fault moving at nearly the same rate as Point Reyes. Note that the 2 mm/yr uncertainty in the tie to the plate framework is comparable to and in many cases larger than the uncertainty in the GPS velocities relative to Point Reyes NCMN.

Velocities for sites in the eastern portion of the network are shown relative to Quincy (Figure 4). Most of these sites were not measured as frequently as the sites in the Coast Ranges. No significant deformation is seen within the network east of Quincy. West of Quincy, all sites move subparallel to the San Andreas fault system. Note that there is significant San Andreas-parallel motion of Orland and other sites in the western Great Valley, relative to Quincy. The implications of this will be discussed in section 5.4.

4. Fault Slip Models

4.1. Dislocation Model

We assume the deformation observed within the network is due primarily to interseismic strain accumulation on the San Andreas fault system. A simple physical model of this system (Figure 5) assumes that the brittle upper crust between earthquakes is locked on the faults approximately to the lower depth limit of seismicity, typically 10-15 km, while the ductile lower crust shears aseismically at the long-term fault slip rates [e.g., *Sibson*, 1982, 1983]. The slip deficit in the upper crust is then recovered during an earthquake. For an infinitely long strike-slip fault this physical model can be represented mathematically by a screw dislocation in an elastic medium, which predicts the fault-parallel surface velocity to be

$$v = (s/\pi)\tan^{-1}[(x - x_f)/D] \quad (1)$$

where s is the steady slip rate, D is the locking depth, x and x_f are the location of the measurement site and fault, respectively [*Savage and Burford*, 1973]. Although this model ignores material heterogeneities, viscoelasticity, and other possibly important effects, it reasonably predicts the first-order features of deformation observed elsewhere along the San Andreas fault system [e.g., *Lisowski et al.*, 1991].

The parameters for even such a simple model may be difficult to resolve. For a model with a single fault, the estimated slip rate and locking depth are highly correlated if the data do not extend at least one or two locking depths from the fault, making models with lower slip rates and shallower locking depth virtually indistinguishable from models with higher slip rates and deeper locking depths [e.g., *Johnson and*

Table 4. Observed Site Velocities, Relative to the Pacific Plate

Site	Velocities, mm/yr						Correlations		
	East	σ	North	σ	Up	σ	E-N	E-V	N-V
0101	17.8	2.8	-33.1	2.2	8.9	11.2	0.0098	0.0102	-0.0252
0102	7.9	3.0	-24.8	2.3	12.7	11.5	-0.0582	0.0592	-0.0559
0103	0.6	2.8	-9.4	2.2	7.9	11.0	0.0110	0.0063	-0.0173
0104	10.2	3.2	-32.1	2.4	0.3	11.9	-0.1160	0.1031	-0.0818
0105	-2.4	2.9	-14.5	2.2	3.2	11.4	0.0178	-0.0013	-0.0102
0106	3.1	6.7	-30.9	3.8	15.8	18.6	0.1781	-0.0848	-0.0902
0108	21.8	7.6	-35.3	4.6	11.8	18.3	-0.3232	0.3037	-0.3196
0109	21.9	6.7	-24.7	4.0	6.0	18.9	0.1349	-0.0184	-0.1051
0114	-3.7	6.2	-5.1	3.7	10.4	16.0	-0.3793	0.2658	-0.2381
01CF	-3.1	19.8	-10.7	8.9	22.9	36.4	0.0885	-0.2078	-0.2207
01EE	2.7	8.8	-14.8	4.2	11.9	21.8	-0.1820	0.1562	-0.2178
01FD	-1.0	12.8	-5.2	5.0	20.4	21.5	-0.0473	0.1725	-0.0802
0220	23.0	6.6	-35.4	3.1	2.2	16.0	0.1975	-0.0466	0.0360
0226	16.9	8.2	-36.3	4.6	2.5	20.3	-0.3994	0.3230	-0.3222
0301	14.2	3.0	-32.0	2.3	14.6	11.5	-0.0487	0.0528	-0.0480
0303	24.8	8.3	-30.3	3.3	1.6	17.6	-0.0094	-0.0881	-0.0102
0306	14.1	5.8	-35.4	2.9	4.7	15.4	0.1012	0.0409	-0.0304
0411	4.3	7.7	-10.6	4.3	9.9	19.9	-0.4073	0.4357	-0.4107
0412	12.9	6.1	-28.4	3.5	15.6	15.4	-0.3345	0.2673	-0.2472
0413	-0.3	3.4	-6.4	2.4	7.3	12.1	-0.1401	0.0942	-0.1121
0414	11.4	3.3	-17.2	2.4	10.6	12.0	-0.1607	0.1062	-0.1159
2ROC	2.2	2.5	-19.1	2.1	5.4	10.7	0.0168	-0.0051	-0.0128
BOYL	2.5	5.5	-9.3	2.7	8.3	14.1	0.0513	-0.0357	0.0042
CHER	5.0	3.2	-19.0	2.3	14.7	11.7	0.0893	-0.0489	-0.0570
CLAR	1.8	2.9	-10.0	2.2	6.1	11.2	-0.0223	0.0119	-0.0270
COLD	5.6	3.2	-14.0	2.3	5.0	11.8	-0.0073	0.0386	-0.0624
CORD	7.6	3.3	-19.6	2.4	15.1	12.0	0.0861	0.0196	-0.0594
DUNN	2.4	5.0	-11.2	2.7	5.0	14.1	0.0105	-0.1079	-0.0648
FIRE	5.6	2.8	-21.3	2.2	7.1	11.1	0.0551	-0.0292	-0.0350
HATC	19.6	3.3	-38.3	2.3	4.3	11.8	0.0182	0.0351	0.0197
HBLF	2.5	3.1	-12.6	2.3	1.7	11.7	0.0923	-0.0376	-0.0569
HOGS	10.2	3.0	-26.3	2.3	19.2	11.6	0.0155	-0.0061	-0.0546
KNEE	17.3	8.7	-28.3	3.9	9.3	20.4	0.1286	0.0062	-0.0497
KOA	4.8	3.2	-18.8	2.3	12.9	11.7	0.0540	-0.0058	-0.0406
LANE	4.3	3.4	-9.4	2.4	11.0	12.0	0.0095	-0.0004	-0.0481
LODO	13.6	3.6	-33.6	2.5	16.2	12.3	-0.2369	0.1740	-0.1439
ORLA	15.2	3.0	-34.4	2.3	20.2	11.5	0.0194	0.0204	-0.0479
PIPE	2.6	3.3	-11.3	2.4	7.7	12.2	0.0416	-0.0218	-0.1031
POLA	16.0	3.9	-36.1	2.5	7.4	12.9	0.0278	0.0625	-0.0187
PRAT	6.4	3.7	-16.4	2.5	-3.9	12.7	-0.0522	0.0347	-0.0276
PRES	9.7	6.2	-15.4	3.7	14.1	17.6	-0.0110	0.0742	-0.2515
PTAR	-1.1	2.4	-4.0	2.1	5.5	10.6	0.0130	-0.0045	-0.0151
PTRY	1.8	2.0	-7.0	2.0	10.6	10.0	0.0000	-0.0000	-0.0000
QUIN	16.3	2.4	-36.8	2.1	11.1	10.5	0.0080	0.0042	-0.0082
RED	10.3	3.6	-24.3	2.5	8.9	12.3	-0.1606	0.1356	-0.1043
REY	3.2	3.2	-24.6	2.3	2.4	12.0	0.0142	0.0149	-0.0628
SAGE	17.4	3.1	-35.9	2.3	4.8	11.6	-0.0181	0.0626	-0.0288
SLID	9.5	2.9	-26.8	2.2	16.4	11.3	-0.0083	0.0223	-0.0286
SPUR	6.9	4.0	-12.1	2.6	5.0	13.1	0.1311	-0.0730	-0.0853
THOM	18.3	3.4	-37.1	2.3	8.0	11.9	0.0273	0.0292	0.0112
UKIA	8.4	2.4	-18.2	2.1	11.3	10.6	0.0153	-0.0031	-0.0142
VAC5	14.8	5.5	-30.8	3.0	29.3	15.1	-0.0902	0.0962	-0.1376
VIEW	16.4	4.2	-39.0	2.6	28.4	13.4	0.0486	-0.0218	-0.0365
FARB	-6.2	2.8	-2.4	2.2	-2.8	11.0	0.0180	-0.0118	-0.0268

East-north-up velocity components are given, along with the sigmas and correlations between components.

Wyatt, 1994]. For the Coast Ranges network the data are particularly limited to the west of the San Andreas fault due to its proximity to the coast. However, using the station velocities relative to the Pacific plate provides an additional constraint, equivalent to adding a station on the stable Pacific plate, that helps to improve the model resolution. For most of the inversions we assumed that we have correctly expressed the velocities relative to the Pacific plate, which means the velocity goes to exactly zero in the far field on the Pacific side of the SAF. We also estimated models assuming the far-field velocity was zero with 2-mm uncertainty to allow for the possibility of a faulty Pacific-fixed frame. In addition, for models with multiple parallel faults, such as in the Coast Ranges, there are high correlations between the slip rates and locking depths on the different faults. Even though the total integrated slip across the fault system is well determined, these high correlations limit our ability to resolve the model parameters for the individual faults.

4.2. Nonlinear Inversion

We wish to determine dislocation models (fault location, locking depth, and deep slip rates) that best explain the

observed surface displacements. If the fault locations and locking depths are assumed to be known, the slip rates are linearly related to the surface displacements so linear least squares estimation techniques can be used. However, in general, the relationship between surface displacements and source model parameters in equation (1) is nonlinear. We use the random cost nonlinear optimization technique [*Berg*, 1993], which we have found to be a computationally efficient method for finding the global minimum in the presence of other local minima that might defeat derivative-based algorithms, such as the Levenberg-Marquardt method [e.g., *Murray et al.*, 1996; P. Cervelli et al., manuscript in preparation, 1998]. Random cost performs a directed Monte Carlo search that mimics a random walk in "cost" space. The cost function we seek to minimize is the mean square error (MSE), which is the weighted L_2 residual norm divided by the degrees of freedom (number of data minus the number of estimated model parameters). Random cost preferentially

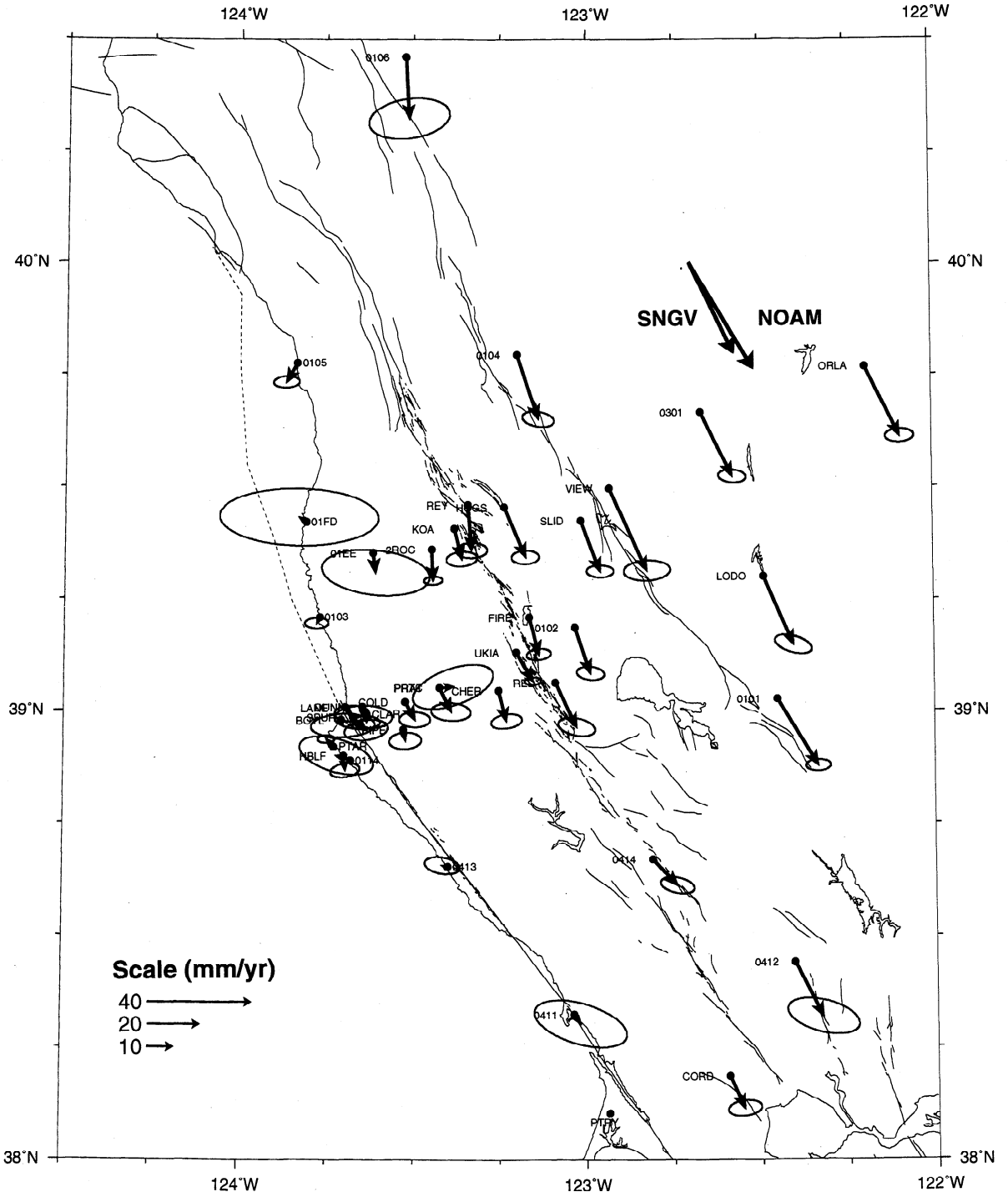

Figure 3. Velocities of sites in the Coast Ranges and western Great Valley, relative to Point Reyes NCMN on the Point Reyes peninsula. Velocities are tipped by 95% confidence regions. Virtually all velocities are parallel to the San Andreas fault system.

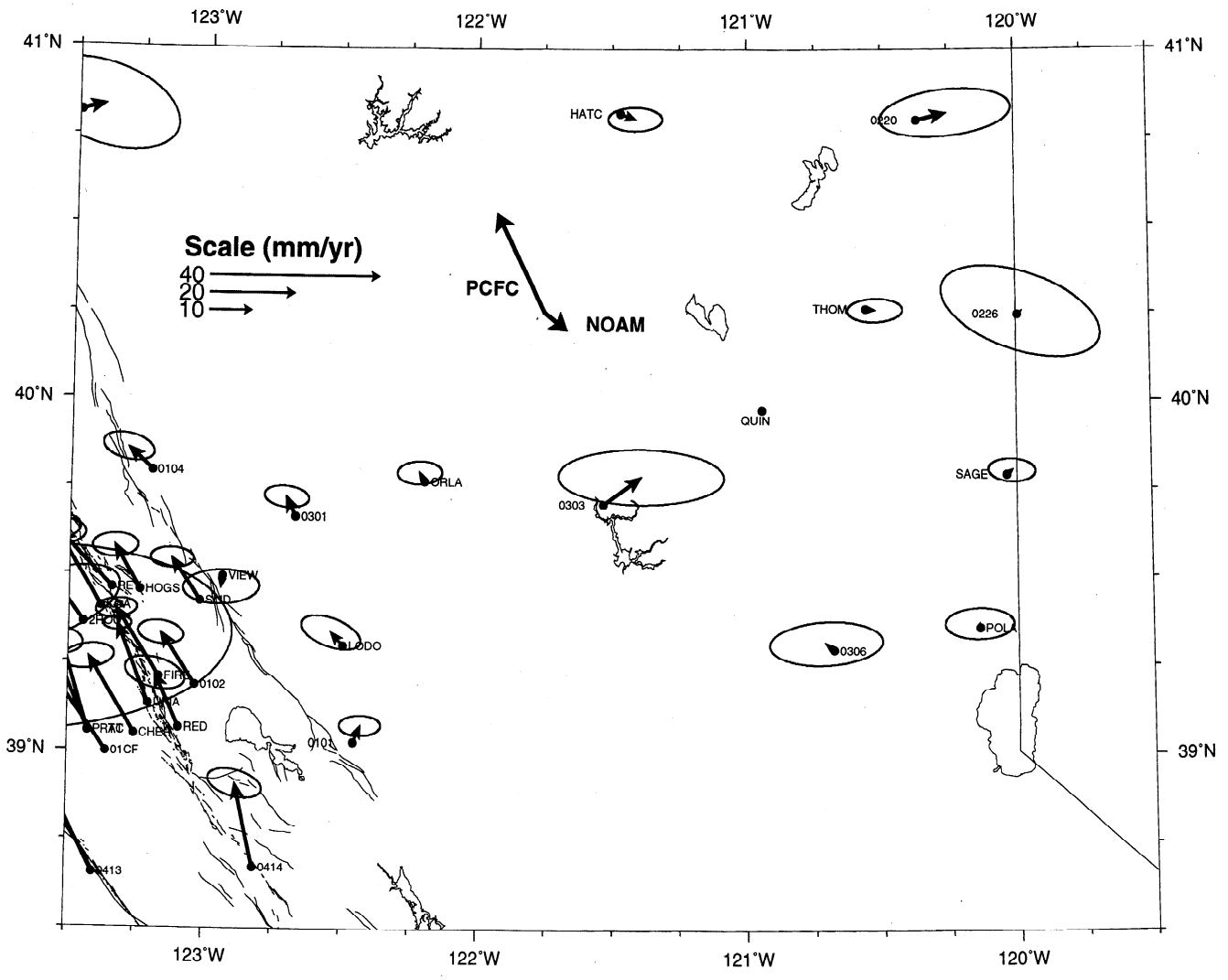

Figure 4. Velocities of sites in the Sierra Nevada, Great Valley, and eastern Coast Ranges, relative to Quincy in the Sierra Nevada. Velocities are tipped by 95% confidence regions. A small amount of right-lateral shear is evident across the Great Valley. No significant deformation is found east of Quincy.

samples the local minima and maxima in cost space while performing the random walk that enables the method to thoroughly search the range of possible models.

We implemented the random cost technique as described by *Murray et al.* [1996] with a few modifications. All parameter values are chosen from the range of physically plausible models. Initially, an a priori model is chosen randomly with uniform probability over the allowable parameter ranges. Alternative trial models are specified using a geometric grid centered on the a priori model. The MSE misfit of the a priori and trial models are computed by forward calculations using equation (1). If any of the trial models has a smaller MSE, a new a priori model is chosen randomly from the trial models using a probability function derived from the MSE differences [see *Berg*, 1993]. This probability function enforces the random walk in cost space and occasionally allows an a priori model with higher MSE to be chosen, which helps to keep the model from converging on an insignificant local minimum of the cost space. The procedure is repeated until none of the trial models has a smaller MSE than the a priori model, which is then assumed to be located at a significant local minimum. However, there is no guarantee that this model is at the global minimum, so the method is repeated several times, each time starting at a different randomly chosen a priori model, to ensure the optimal model with the global minimum MSE is found.

Because the geodetic inverse problem is nonlinear, the confidence regions associated with the estimated parameters do not follow a Gaussian probability distribution and thus are not necessarily symmetric, even though the noise associated with the input velocity data vectors (their covariance) is assumed Gaussian. Therefore, to assess how well the model parameters are resolved by the data, we used the bootstrapping method [e.g., *Efron and Tibshirani*, 1986], which in general makes no assumptions about the probability density function of the data or the model parameters. Bootstrapping is performed by repeatedly estimating model parameters from randomly resampled data. We used random cost to estimate models from the resampled data, using the previously determined optimal model as the initial a priori model to improve convergence. Bootstrapping techniques usually treat the data as equally weighted and uncorrelated. In our case, the data to be modeled are the station velocities estimated from GPS data for which we have some estimate of their uncertainty and correlations.

Although the estimated velocity covariance matrix assumes a Gaussian probability distribution that probably only approximates the true velocity uncertainties, we wish to use this additional information to provide better constraints on the uncertainties of the fault model. Therefore we have modified the bootstrapping technique to apply the resampling to data that has been normalized (equally weighted and uncorrelated) by its covariance.

We use the following methodology to ensure that each random cost determination is based on the same resampled data during each bootstrap iteration. At the start of a bootstrapping iteration, we define a square matrix operator $\mathbf{J}$, composed of zeros and ones, that performs a random resampling of the data vector $\mathbf{d}$, $\mathbf{d}^* = \mathbf{J}\mathbf{d}$, where the asterisk denotes resampling. For each trial model we determine the unweighted residuals $\mathbf{r}$ corresponding to the original data $\mathbf{d}$ and compute normalized residuals using the (symmetric) inverse square root of the data covariance $\mathbf{C}_d$, $\hat{\mathbf{r}} = \mathbf{C}_d^{-1/2}\mathbf{r}$. The normalized residuals $\hat{\mathbf{r}}$ are uncorrelated and have uniform weight and can be resampled independently: $\hat{\mathbf{r}}^* = \mathbf{J}\hat{\mathbf{r}}$. The resampled residuals are used to determine the MSE differences for picking the next a priori model in the random cost run. The same resampling operator $\mathbf{J}$ is used for an entire bootstrapping iteration, and then a different resampling operator is randomly chosen for the next bootstrap iteration.

We ran 10,000 bootstrap models to estimate the confidence region for the model. The range of the resulting bootstrap models provides a good approximation to the confidence region of the original estimated model. We determined the two-sided confidence intervals at the $1-\alpha$ level for each parameter

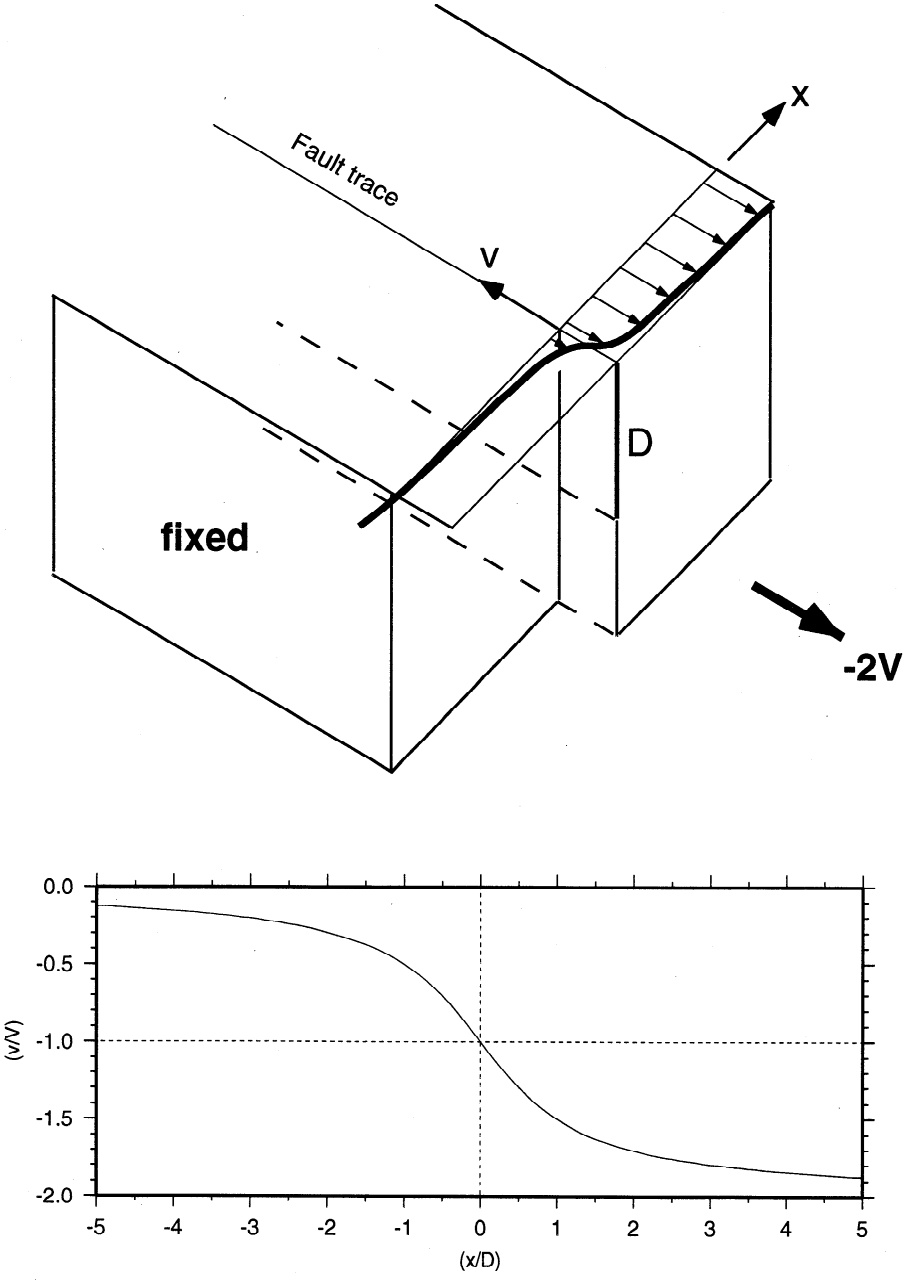

Figure 5. Fault model. Below a depth D, the far side of the fault moves to the right at speed $2V$, while the fault remains locked from depth D to the surface. The predicted surface velocity field is shown by a solid line.

by the bootstrap percentile method in which the N estimated values are numerically ordered and the upper and lower limits are given by the $N\alpha/2$ and $N(1-\alpha/2)$ values, respectively from the ordered list (for 10,000 resampled models, the 95% confidence limits are given by the 250th and 9750th values) [e.g., *Arnadóttir and Segall,* 1994]. We determined the full confidence region of the model, which provides useful information about the correlations between different parameters, by numerically ordering the resampled MSE, and choosing the $N(1-\alpha)$ value from the ordered list as the limit. Any model whose MSE is less than the limit value is not significantly different than the optimal model at the $1-\alpha$ level. P. Cervelli et al. (manuscript in preparation, 1998) provides additional details about our implementation of the random cost and bootstrap methods.

We use the velocities relative to the Pacific plate from 31 stations from Point Arena to Quincy and HPGN 0306 in the Sierra to estimate the optimal model. We assume that physically plausible dislocation models could have right-lateral slip rates ranging from 0 to 40 mm/yr and locking depths ranging from 0 to 100 km on each fault, so that each fault could accommodate the observed total integrated plate slip rate and locking depths could extend well below the observed seismogenic depth. All model parameters were randomly chosen, rather than estimating slip rates linearly after the fault geometry parameters were randomly chosen as was done by *Murray et al.* [1996], because simulations by P. Cervelli et al. (manuscript in preparation, 1998) suggest that convergence in the random cost method can be degraded when some parameters are linearly estimated. The uncertainties for models in which all parameters were allowed to vary were so large that no useful information could be determined about the individual parameters. Therefore we assumed the fault locations are reasonably well determined from geologic maps and estimated only the fault slip rates and locking depths.

We allowed each random cost run to iterate 1000 times on the a priori model, using about 100 trial models during each iteration. If multiple local minimum models were located, we chose the optimal model found during the run. We repeated this procedure several times, each time determining essentially the same optimal model, indicating that the cost space has a well-defined minimum. The optimal model and confidence intervals for the six fault parameters are summarized in Table 5. The optimal model had an MSE of 1.04, not significantly different from the expected 1.00 if both the model and the errors are realistic. We also tested a model that does not require zero velocity in the far-field, but includes an additional velocity constraint 0±2 mm/yr at 150 km SW of Point Arena to

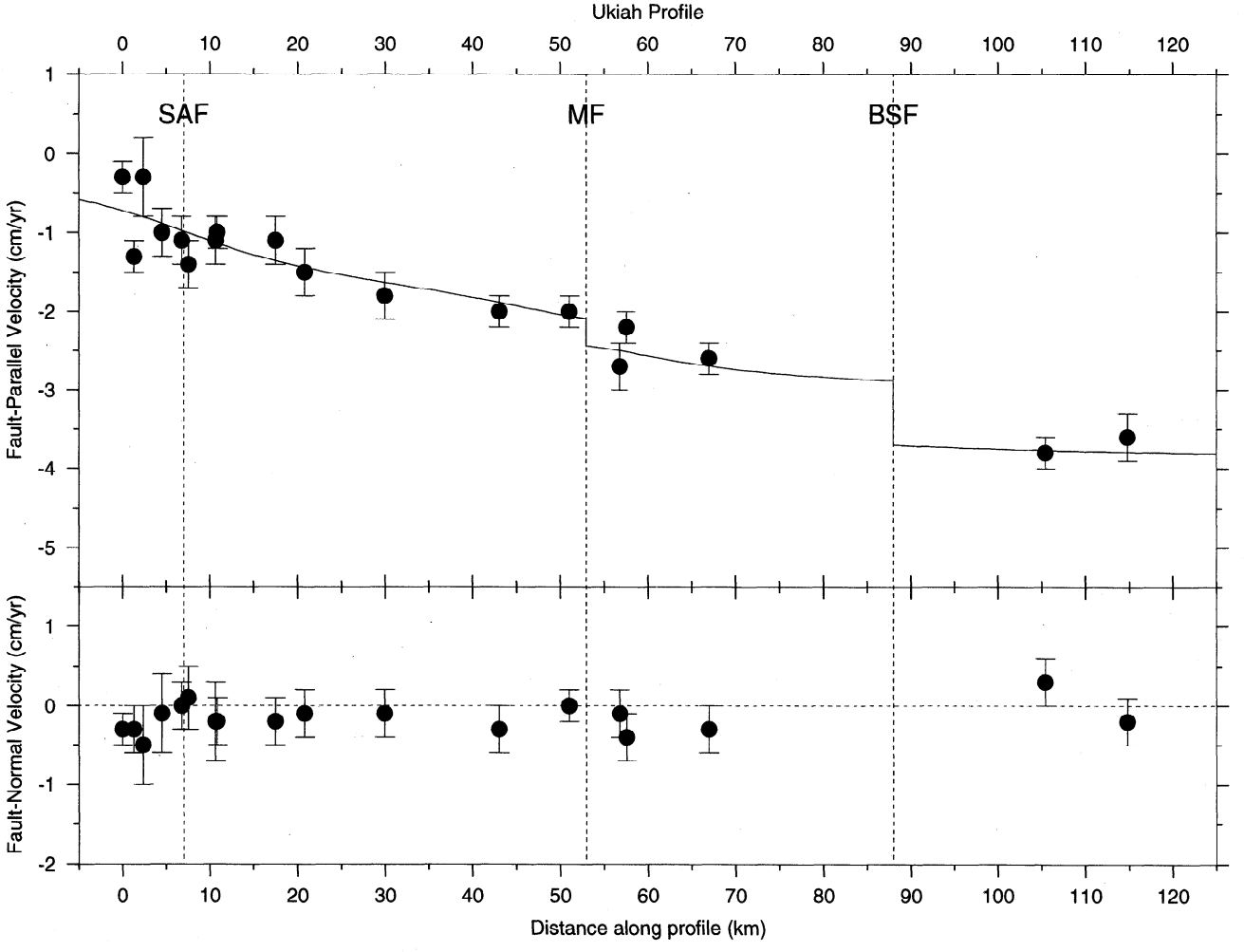

Figure 6. Ukiah profile. Fault-parallel velocities are shown along with the predictions of the optimal model. Fault-normal velocities were not modeled but are shown for reference. While total the fault-parallel slip is 40 ± 1 mm/yr, only 3 ± 2 mm/yr of fault-normal shortening is observed between the Great Valley and Pacific coast.

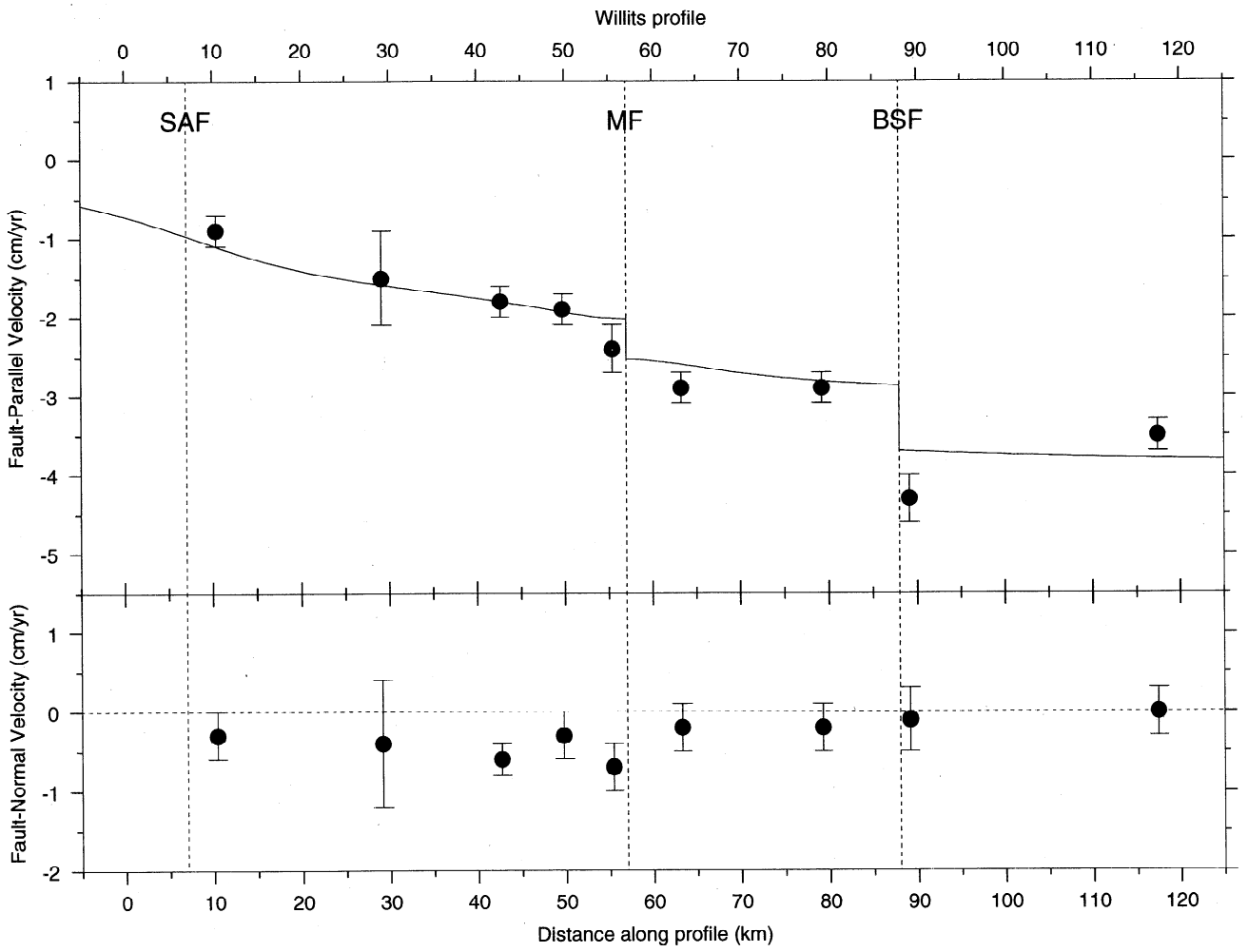

Figure 7. Willits profile. Fault-parallel velocities are shown along with the predictions of the optimal model. Fault-normal velocities were not modeled but are shown for reference.

represent the stable Pacific plate. This alternate model would be preferred if our realization of a Pacific-fixed frame was faulty.

4.3. Fault Geometry

Because the three faults in the vicinity of Ukiah and Willits are nearly parallel, we use a two-dimensional, three-fault dislocation model to estimate slip rates for the three faults of the San Andreas system. We analyze two profiles normal to the fault system, a southern profile through Point Arena and Ukiah (Figure 6) and a northern profile through Willits 40 km to the north (Figure 7). The geometries for these models are slightly different, as the faults are located in slightly different locations along the profiles. The change in geometry is necessary because all three faults change strike from south to north. The differences in fault location are only a few kilometers but are important since we have data from sites very close to the faults. We inverted the two profiles both separately and jointly to test for the possibility that slip rates may vary along strike. The misfit of the model with separate slip rates for each profile is marginally lower than the model with constant slip rates throughout the region, but the improvement is small enough that the three additional model parameters are not required by the data. In all models presented here the fault slip rates are assumed to be the same for both profiles.

An additional complication arises for the Ma'acama fault, as there is clear evidence for fault creep at the surface along several segments of the fault. The measured creep rate on the Ma'acama fault at Willits is 5.1 ± 0.8 mm/yr and at Ukiah is 3.5 ± 1.9 mm/yr [*Galehouse*, 1994]. Surface fault creep can be modeled by adding screw dislocations with the appropriate geometry to the fault model. The northern Hayward fault, of which the Ma'acama fault is an along-strike continuation, also creeps at 4–6 mm/yr [*Lienkaemper et al.*, 1994]; *Savage and Lisowski* [1993] inferred a 5 ± 1 km depth of the creeping zone from a friction model of fault slip driven by stress induced by deep slip on the San Andreas, Hayward, and Calaveras faults. We investigated the possibility of estimating creep rates from the GPS velocities, but the data strength is insufficient to determine creep rates along with the other parameters. We model the shallow creep using screw dislocations, assuming a 5-km depth limit for creep and the above creep rates, and subtract the surface displacements due to creep from the data prior to estimating the fault parameters.

4.4. Optimal Model

The optimal model (Table 5) and its uncertainties provide new constraints on the both slip rates and locking depths in San Andreas fault system. Upper and lower bounds quoted in this section are based on 95% confidence intervals. The San Andreas fault is locked to at least 5 km depth, and the

Table 5. Estimated Fault Slip Rates and Locking Depths and Their Confidence Intervals

	Pacific Plate Velocity Constraint			
	0 mm/yr			0 ± 2 mm/yr
Parameter	Optimal	68.6% Confidence	95% Confidence	Alternate Model
SAF depth	14.9	7.8–27.4	4.7–44.6	18.2
MF depth	13.4	8.6–20.8	4.4–29.0	12.2
BSF depth	0.0	0.0–5.1	0.0–32.0	0.0
SAF slip rate	17.4	14.3–19.9	10.5–22.6	20.7
MF slip rate	13.9	11.1–18.0	7.8–24.4	12.0
BSF slip rate	8.2	6.3–10.3	3.8–13.0	8.5
Total slip rate	39.6	39.0–41.1	38.1–42.2	41.1

All parameters were estimated by nonlinear optimization. Confidence regions were chosen from 10,000 bootstrap runs. The optimal model has a mean square error of 1.04. Locking depths given in km; slip rates given in mm/yr.

Ma'acama fault is locked to at least 4 km. Both of these faults have a deeper locking depth than the Bartlett Springs fault. Models in which the Bartlett Springs fault creeps in a rigid block fashion are favored. Maximum (95% confidence) locking depths for all faults are deeper than the seismogenic zone and are poorly resolved by the data. In the optimal model (Table 5) the San Andreas fault accommodates about 45% of the total slip on the system, the Ma'acama fault accommodates about 35% and Bartlett Springs fault accommodates about 20%. The total slip rate is better resolved than the individual fault slips, which reflects the high negative correlations between slip parameters shown in Figure 8. Strong correlations are also found between locking depth parameters. Correlations are strongest between adjacent faults and are less pronounced between the San Andreas and Bartlett Springs faults. The 95% confidence region includes models in which virtually all slip is found on the Ma'acama fault; such a model has a locking depth of 41.5 km on the Ma'acama fault, and the misfit is not too high because the velocity gradient is so smooth across the Coast ranges and approximately antisymmetric about the Ma'acama fault. The 95% confidence regions would shrink considerably if, for example, we required locking depths to be bounded within 0-20 km rather than 0-100 km; 68.6% confidence intervals for the slip rates would not be changed very much. That the total slip rate is determined more precisely than the individual fault slip rates is a consequence of the multiple parallel strike-slip faults, not the inversion method; the same result is found in linear inversions where only slip rate is estimated. We get similar results from an alternate model, in which the far field on the Pacific plate is not required to go to zero but is constrained to 0 ± 2 mm/yr 150 km west of the San Andreas fault (Table 4). The alternate model gives 41 mm/yr total slip, with a slightly higher slip rate and locking depth for the San Andreas fault, and a slightly lower slip rate for the Ma'acama fault. Results for the Bartlett Springs fault are not affected by the differences in the model.

5. Discussion

5.1. *Total Slip on the San Andreas Fault System*

Our estimate of the total slip rate on the San Andreas fault system at latitude 39-40°N is $39.6^{+1.5}_{-0.6}$ mm/yr. We indicate estimates and 68.6% confidence intervals from the nonlinear inversion in a compact form using a superscript to indicate the upper end of the confidence interval and a subscript to indicate the lower end. In this convention, $39.6^{+1.5}_{-0.6}$ indicates an optimal estimate of 39.6 with a 68.% confidence interval spanning (39.6-0.6, 39.6+1.5). This estimate is greater than the predicted motion of the Sierra Nevada–Great Valley block, 37-38 mm/yr [*Argus and Gordon*, 1991; *Dixon et al.*, 1995], but the 95% confidence regions overlap. It is also consistent with geologic slip rates. *Kelson et al.* [1992] summed slip rates over four separate paths from the Great Valley to the Pacific coast. The total slip rate estimated for their northern path, slightly to the south of our study area, is 39.8 ± 5.3 mm/yr. They found little variation in the total slip rate of the San Andreas system along strike, the variation being significantly smaller than the stated uncertainties of 5-6 mm/yr.

Our estimate of the total right-lateral shear between the Pacific coast and the Great Valley is in good agreement with that inferred from previous studies using data from the latitude of Point Reyes. The total right-lateral shear measured by 18 years of Geodolite data was 31 ± 3 mm/yr, based on a network spanning 115 km from the Farallon Islands to the western edge of the Great Valley [*Lisowski et al.*, 1991]. *Williams et al.* [1994] estimated 33 ± 2 mm/yr between the Farallon Islands and station CAML at the western edge of the Great Valley. If we use the average of the three easternmost sites of their profile to define the velocity of the western edge of the Great Valley we find 28 ± 2 mm/yr between Point Reyes NCMN and the western edge of the Great Valley. In comparison, if we define the western edge of the Great Valley using sites 0101, 0301, and LODO, our estimate is 29 ± 2 mm/yr, an insignificant

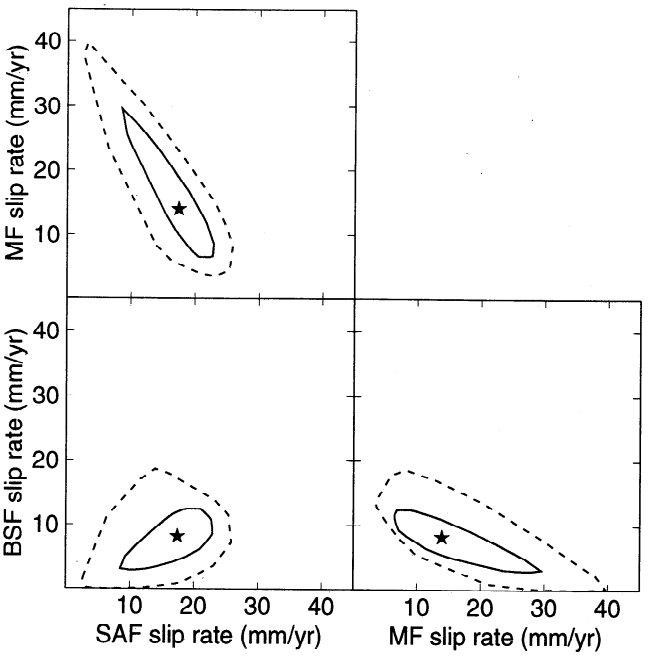

Figure 8. Optimal model and confidence regions for slip rates, showing correlations between the San Andreas (SAF), Ma'acama (MF), and Bartlett Springs (BSF) faults. The star indicates the optimal model. Confidence regions are indicated with contours: solid for the 50% confidence region and dashed for the 95% confidence region. Note the strong correlations between slip rates on adjacent faults, SAF and MF, and MF and BSF.

difference. We find no evidence for any along-strike change in the total slip rate on the San Andreas fault system.

5.2. *Individual Fault Slip Rates*

We compare our estimated slip rates to geological estimates, and our estimated locking depths for each fault with the observed lower depth limit of seismicity.

5.2.1. San Andreas fault. Geologic slip rate estimates are available only for the SAF, suggesting a slip rate of 20-25 mm/yr on the North Coast segment [*Niemi and Hall*, 1992; *Prentice*, 1989]. Our model slip rate is $17.4^{+2.5}_{-3.1}$ mm/yr. The 68.6% confidence region is lower than all estimated geologic slip rates, although the 95% confidence region of 10.5-22.6 mm/yr overlaps the range of geologic estimates. The SAF slip rate is sensitive to the reference frame assumptions and is larger by about 3 mm/yr in the alternate model, which would put it in better agreement with the geologic estimates. Our estimate of SAF slip rate could be improved significantly by including data from offshore sites, only possible to the south of the study area, or by a more precise realization of a Pacific plate-fixed reference frame that would decrease reference frame uncertainties.

The San Andreas slip rate on the San Francisco Peninsula is thought to be 17 ± 3 mm/yr [Working Group on Northern California Earthquake Potential (WGNCEP), 1996]. However, if one includes the San Gregorio fault (slip rate of 5 ± 2 mm/yr), the combined faults slip at a rate of 22 ± 4 mm/yr. South of the San Francisco Bay the San Andreas is estimated to slip at a rate of 22 ± 6 mm/yr [*Kelson et al.*, 1992] and the combined San Andreas–San Gregorio slip rate is 27 ± 6 mm/yr. Neither estimate is significantly different from the slip rate on the North Coast segment of the San Andreas determined by geodesy or paleoseismic studies. Given the large uncertainties in the geologic slip rate estimates, we feel justified in assuming that the San Andreas slip rate does not change along strike. Our results suggest that the lower range of the geologic estimates may be more realistic unless the slip rate is actually decreasing to the north.

There has been virtually no seismicity on the San Andreas fault since the 1906 earthquake, but other geodetic data provide independent estimates of the locking depth. At Point Arena a dense triangulation network was surveyed before and after the 1906 earthquake, making this location one of the best to study slip in that earthquake. *Thatcher* [1975] suggested that the maximum depth of coseismic slip in 1906 was constrained to be 10 km or less, assuming uniform slip with depth on the fault. *Matthews and Segall* [1993] invert for the depth distribution of slip assuming that the slip varies smoothly and show that significant slip occurred as deep as 15 km, or possibly 20 km. *Thatcher et al.* [1997] point out that the models of *Matthews and Segall* [1993] do not require more than 30% of the surface slip at any depth greater than 10 km.

Our optimal model has a locking depth of 14.9 km, more consistent with the suggestion of *Matthews and Segall* [1993]. The lower limit on the locking depth is well constrained, but the upper limit is not. A deep locking depth for the San Andreas fault at Point Arena is also consistent with other data. In 1991 and 1992 we reoccupied a small-aperture EDM network surveyed in the 1980s at Point Arena. Virtually all fault-crossing lines with lengths of 1-5 km changed length by less than 10 mm in the 8 years between surveys, with typical line length rates of change of 1 mm/yr or less (Table 6). This network measures the strain rate in the immediate vicinity of the fault, which is a simple function of the slip rate and locking depth. We used the GPS-EDM line length changes to estimate the locking depth for three different slip rates, 15, 20, and 25 mm/yr (Figure 9). Shallow locking depths are clearly ruled out by this data, but the optimum value and upper bound on the locking depth are poorly constrained. A small-aperture network can place constraints on the minimum permissible locking depth but not the maximum.

Table 6. Short-range EDM data from Point Arena

Site 1	Site 2	Date	EDM Dist., m	GPS Dist., m	Rate, mmyr	σ, mm
BIAG	OZ	June 10, 1977	755.975	755.989	1.02	0.23
BIAG	RICK	June 10, 1977	1057.896	1057.893	-0.22	0.23
BIAG	SCHU	June 10, 1977	964.081	964.088	0.51	0.32
OZ	RICK	June 10, 1977	1723.439	1723.435	-0.30	0.23
OZ	SCHU	June 10, 1977	1228.211	1228.213	0.12	0.28
RICK	SCHU	June 10, 1977	903.506	903.512	0.46	0.25
BOYL	LANE	Sept. 27, 1983	3268.606	3268.595	-1.24	0.43
CBLE	SHOE	Sept. 26, 1983	2614.967	2614.982	1.79	0.58
BOYL	SPUR	Sept. 20, 1983	3099.860	3099.858	-0.27	0.57
CLAR	DUNN	Sept. 28, 1983	2215.566	2215.562	-0.52	0.46
GONZ	LANE	Sept. 28, 1983	5419.447	5419.450	0.40	0.49
GONZ	SHOE	Sept. 28, 1983	5510.157	5510.133	-2.91	0.51
GONZ	SPUR	Sept. 28, 1983	3396.889	3396.880	-1.06	0.51
HBLF	PTAR	Sept. 20, 1983	3404.822	3404.831	1.06	0.48
LANE	SHOE	Sept. 27, 1983	4844.932	4844.923	-1.07	0.44
SHOE	LANE	Sept. 27, 1983	4844.932	4844.923	-1.07	0.44
LANE	SPUR	Sept. 20, 1983	3114.877	3114.878	0.12	0.47
SHOE	SPUR	Sept. 20, 1983	2620.765	2620.752	-1.62	0.44

The date of the first EDM measurements is given, along with the EDM measured distance, GPS measured distance, and the line length rate of change and sigma. Site locations are shown on Figure 9b, along with the 1991-1995 GPS velocities for sites with enough GPS data. GPS measurements from July 1991 and July 1992 were used to derive line length rates.

5.2.2. Ma'acama fault. No geological slip rates have been estimated for the Ma'acama fault, but *Schwarz et al.* [1992] estimated the slip rate for the Rodgers Creek fault, its extension to the south, as 6.4 to 10.4 mm/yr. Our estimate of $13.9^{+4.1}_{-2.8}$ mm/yr is higher than this rate, and also above the similar slip rate on the Hayward fault to the south [*Lienkaemper et al.*, 1994]. Again, we cannot exclude the geologic rate at 95% confidence. Our estimated slip rate is considerably higher than the rate of shallow creep observed along the fault, suggesting that the shallow creep relieves only a fraction of the tectonic stress. No large earthquakes have occurred on the Ma'acama fault within the historical record, but its long-term seismic potential must be at least as great of that of the Hayward fault to the south. Based on fault length and slip rate, it seems likely that the Ma'acama fault is capable of generating magnitude 7 earthquakes. In the roughly 150 years of the historic record, the Ma'acama fault has accumulated a slip deficit of >2 m. Without an estimate of the average recurrence time, an accurate estimate of the probability of the next such earthquake occurring within the next 30 years is not possible, but the slip deficit is at least large enough to generate a magnitude 7 earthquake today. For the Ma'acama fault the observed base of the seismogenic zone is 10-12 km and is fairly uniform along strike throughout the study area [*Castillo and Ellsworth*, 1993]. This compares very well with our optimal locking depth of 13.4 km.

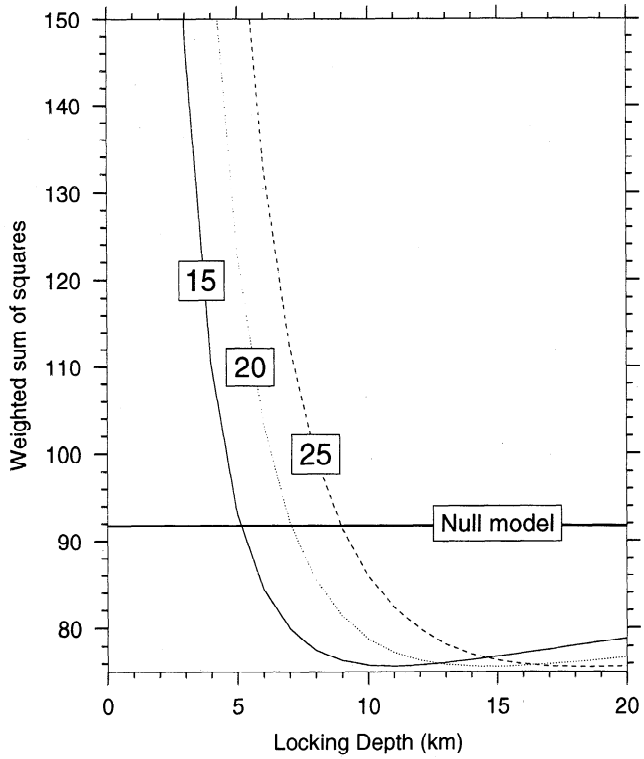

Figure 9a. The weighted sum of squares misfit of a model to observed GPS-EDM line length changes at Point Arena is plotted for three different assumed fault slip rates, 15, 20, and 25 mm/yr. The horizontal line labeled "Null model" is the misfit if no deformation is assumed. Best fitting locking depths are 11, 15, and 18 km, respectively, but all minima are very broad as the near-fault network places very weak constraints on the upper limit for locking depth. Nevertheless, the minimum acceptable locking depth from the EDM data agrees well with the GPS locking depth estimates.

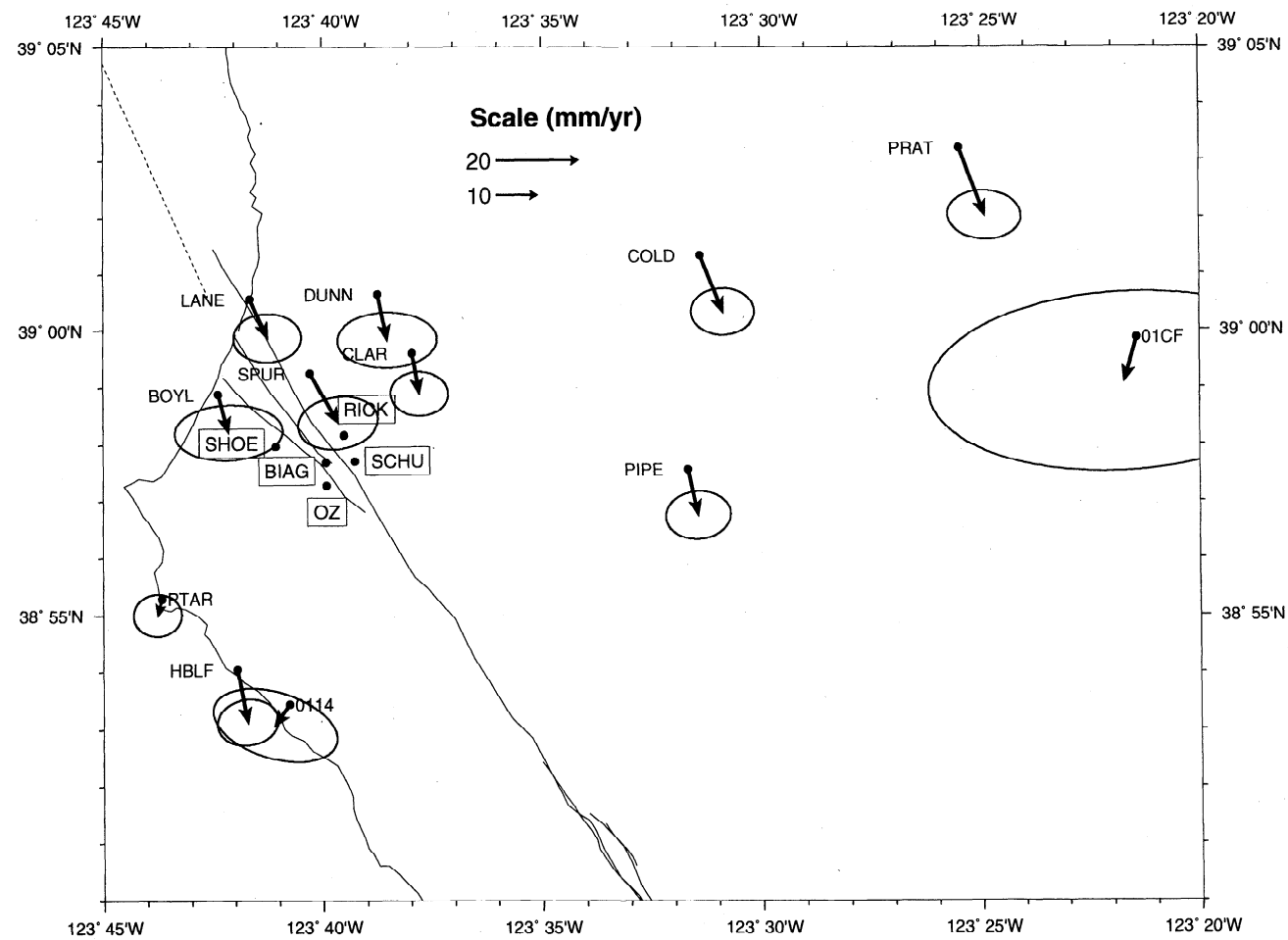

Figure 9b. GPS velocities 1991-1995 for sites near Point Arena, relative to the Pacific plate. Dots labeled with names in boxes indicate EDM sites used in Figure 9a that do not have enough GPS data to derive precise velocities.

5.2.3. Bartlett Springs fault. Similarly, no slip rate has been estimated for the Bartlett Springs fault, but the Green Valley fault, its presumed extension to the south, has been shown to creep at 5 mm/yr [*Frizell and Brown*, 1976]. Our estimate of $8.2^{+2.1}_{1.9}$ mm/yr of (aseismic) slip is slightly higher; the 95% confidence interval contains the geologic estimate, although the 68.6% confidence interval does not. The Bartlett Springs fault is probably not capable of generating magnitude 7 earthquakes, as it appears that most tectonic strain is released through creep. The sum of our Ma'acama and Bartlett Springs fault slip rate estimates is in good agreement with the total right-lateral shear observed across those two faults in the Covelo and Geysers Geodolite networks, about 20 mm/yr (M. Lisowski, personal communication, 1991).

Seismicity on the Bartlett Springs fault is much less uniform along strike [*Castillo and Ellsworth*, 1993]. Almost no seismicity is observed over large areas of the fault. South of the edge of the Gorda slab, there are discrete clusters of seismicity extending to 10 km depth below Round Valley (vicinity of site 0104), to 15 km depth beneath Lake Pillsbury, and to 7 km depth near Clear Lake. Our optimal model has the Bartlett Springs fault creeping over its entire depth, and the 68% confidence region for the BSF locking depth spans 0–5.1 km. This results mainly from the sites in the vicinity of Lake Pillsbury. Slide and View, located 5 km on either side of the fault, have fault-parallel velocities that differ by 14 ± 2 mm/yr in a right-lateral sense (Figure 7). The average shear strain rate between Slide and View is significantly higher than that between any two sites a similar distance apart across the San Andreas or Ma'acama faults. Because these are the only two sites close to the BSF, our finding of creep on the BSF is well established only in the vicinity of Lake Pillsbury.

5.3. Implications for the Development of the San Andreas Fault System

Furlong and coworkers [*Furlong et al.*, 1989; *Furlong*, 1993] have suggested based on thermal models that the plate boundary in the mantle may be offset to the east from the plate boundary at the surface. They argue that shear will gradually become more localized to the east with distance south from the Mendocino triple junction. In the San Francisco Bay area, shear in the upper mantle will be localized beneath the Hayward fault, ~40 km east of the SAF. They suggest the SAF is connected to this deeper shear zone by a subhorizontal detachment at about 20 km depth.

One might anticipate that the slip rate on the San Andreas would thus decrease with distance south from the triple junction, as deformation was transferred to the Hayward-Ma'acama fault system. There is no evidence in the geodetic or geologically determined slip rates to suggest this, although the uncertainties are quite large. Our estimated slip rate for the SAF is lower than the geologic estimates, and our slip rate for the Ma'acama fault is higher than that estimated in the San Francisco Bay area to the south. Given the uncertainties, our results are consistent with no change in slip rates along strike; our results argue against the slip rate on the SAF decreasing from north to south.

Our modeling results do not argue for or against a detachment connecting the SAF to a deeper plate boundary. *Prescott and Yu* [1986] and *Lisowski et al.* [1991] have emphasized that rather different kinematic models of fault structure in the lower crust and upper mantle cannot be distinguished on the basis of geodetic slip rates alone. We note, however, that recent deep crustal seismic reflection data suggest that the strike-slip faults in the Coast Ranges cut vertically through the entire crust [*Hole et al.*, 1998]. The argument that there is an offset between the surface plate boundary and the mantle plate boundary [*Furlong et al.*, 1989; *Furlong*, 1993] presupposes that the SAF is the main expression of the plate boundary. Our optimal fault slip rate estimate for the slip rate for the SAF is only slightly higher than that for the MF and <50% of the total slip; even if we use the 95% confidence upper bound for the SAF slip rate, it has no more than about 55% of the total slip on the San Andreas system.

5.4. Shortening Across the Coast Ranges

Significant shortening is not apparent across the Coast Ranges within this network. A quantitative assessment of shortening is complicated by the fact that the faults of the San Andreas system change strike by as much as 15-20° within the study area, with the faults striking more northerly near the Mendocino triple junction. A change of a several degrees in the definition of the "fault-parallel" component of the velocities can change the estimate of the fault-normal component by up to a few millimeters per year. The rate of shortening across the Coast Ranges, between the Pacific coast (stations Point Arena, 0413 and Point Reyes) and the Great Valley (stations Orland, 0301, View, Lodoga and 0101), is 3 ± 2 mm/yr at an azimuth of N60°E. Site 0101 in the easternmost Coast Ranges moves 3 ± 2 mm/yr to the northeast relative to Orland in the Great Valley. *Unruh et al.* [1992] estimated a contraction rate of 1-3 mm/yr across the Rumsey Hills and Dunnigan Hills, located to the east of site 0101. No significant contraction normal to the Coast Ranges is required between site 0101 and sites at the same latitude on the Pacific coast. Additional surveys over a longer time period will be required to accurately determine the rate of fault normal shortening.

5.5. Azimuth Changes

Gilbert et al. [1994] showed that the orientation of maximum shear for several terrestrial geodetic networks along the SAF was better predicted by local fault strike than by the direction of relative plate motion. Based on this observation, they argued that geodetic data along the SAF favored models dominated by vertical structures, in which crustal faults are underlain by ductile shear zones of the same orientation that localize shear beneath the surface trace of faults, as opposed to models including horizontal detachments in which crustal faults of varying orientations cut an elastic plate overlain by a ductile medium that undergoes shear oriented in the direction of relative plate motion. GPS results from the Coast Ranges network are sufficiently precise that we can consider whether individual site velocities are better predicted by local fault strike or by the direction of plate motion. Below we examine changes in the azimuth of the observed site velocities, which represent the deviations from the two dimensionality assumed in sections 5.1 through 5.3. While the strain orientations used by *Gilbert et al.* [1994] were derived from networks spanning 30-50 km and thus represent spatial averages over such an area, the GPS velocities allow a similar test to be made without

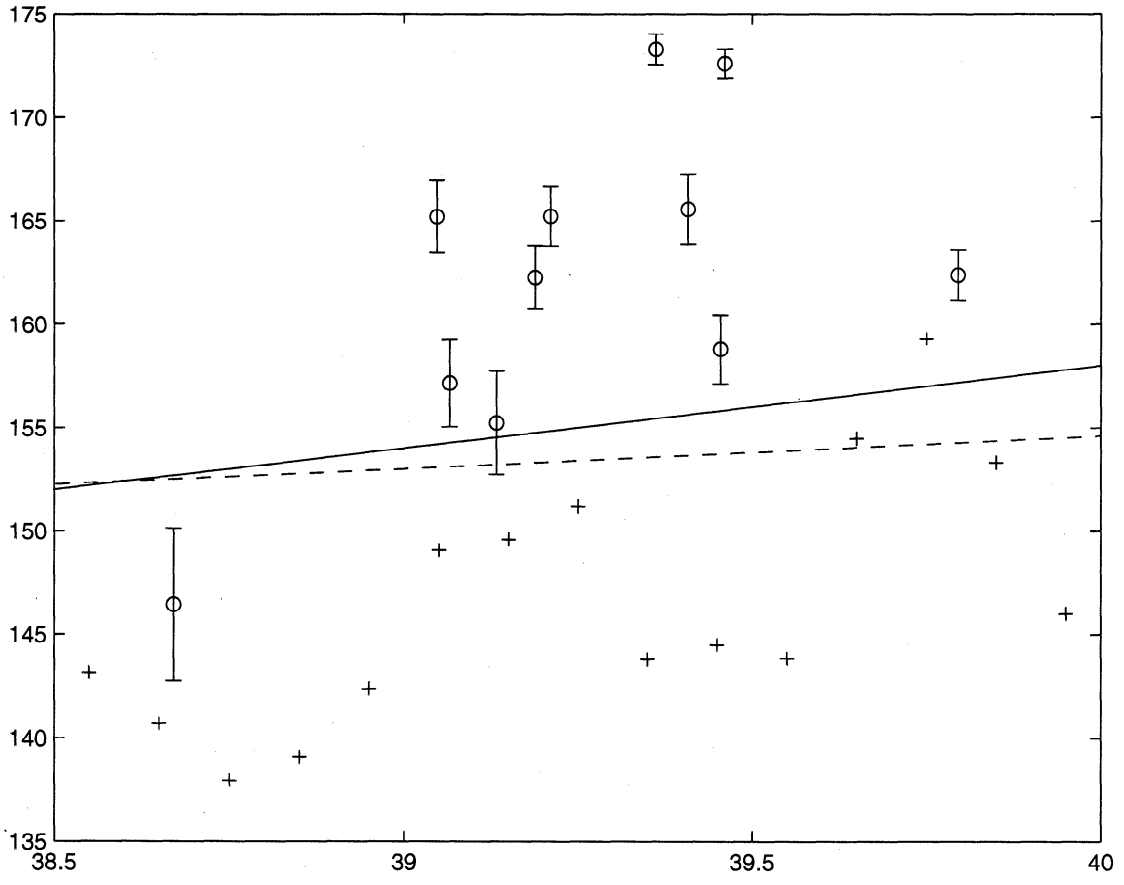

Figure 10. GPS azimuths (circles with 1σ error bars), local fault strikes (crosses), and directions of SNGV-PCFC relative motion (solid and dashed lines) as functions of latitude. All refer to the Ma'acama fault. The solid line refers to the pole SNGV-PCFC$_1$, while the dashed line refers to the pole SNGV-PCFC$_2$; both are included to give an indication of the range of plausible plate motion directions. As little as 3 mm/yr of fault-normal shortening between the Great Valley and Coast Ranges can reconcile the fault slip rates and plate motion directions. Errors in the GPS reference frame could be responsible for the misfit between the GPS azimuths and plate motion predictions, since both change similarly with latitude.

such spatial averaging and with station spacing smaller than the average lithospheric thickness.

From north to south a systematic change in azimuth is clearly visible for velocities of sites within the Coast Ranges (Figure 3). We examine the change in azimuth as a function of latitude for the 11 sites near the Ma'acama fault. All of the selected sites move at similar rates relative to the Pacific plate. The azimuths of the velocity vectors (relative to Pacific) change systematically from 162° ± 4° for site 0104 in the north to 146° ± 7° for site 0414 in the south (Figure 10). The difference in azimuth between sites 0104 and 0414 is 16° ± 8°. The strike of the Ma'acama fault also changes with latitude, with the strike rotating by 10-15° between the latitudes of sites 0104 and 0414, and the direction of relative plate motion changes by a similar amount. Figure 10 shows the azimuths of the velocity vectors for sites near the Ma'acama fault as a function of latitude, compared to the local fault strike and the azimuth of SNGV-PCFC relative motion computed using two different SNGV-PCFC poles to illustrate the uncertainty in plate directions associated with this boundary.

All three sets of azimuths show a similar dependence on latitude, but there are systematic offsets between the three sets. The average fault strikes, expressed as azimuths clockwise from north, are systematically smaller than the SNGV-PCFC relative plate motion, which is systematically smaller than the observed GPS azimuths. The offset between the fault strikes and plate motion directions can be reconciled if we assume 2-3 mm/yr of fault-normal contraction occurs between the Coast Ranges and Great Valley, as suggested above in the GPS results. Using the SNGV-PCFC$_2$ pole, the contraction required to explain the azimuth difference is smaller and is required only south of 39.5°N.

The systematic offset between the GPS azimuths and the plate motion direction might be due to a systematic bias in relating the velocities to the Pacfic plate or in the motion of the SNGV relative to the Pacific plate; an SAF-normal bias of 2-3 mm/yr would be enough to bring the azimuths into agreement. Given the uncertainties in the plate motion that result from the poor constraints on SNGV motion and the similar rate of change of azimuth with latitude, we cannot tell whether site velocities are better predicted by local fault orientation or plate motion direction. In fact, the local fault orientation may be a result of the deep flow patterns related to plate motion. Because the change in the azimuth of the relative plate motion is predicted to be 5-10° over only 200 km, depending on the pole used, we suggest that a better

determination of the Pacific-Sierra Nevada relative motion may be critical to understanding the changes in fault strike observed in the northern Coast Ranges.

5.6. Sierra Nevada–Great Valley Block

Observed velocities within the Sierra Nevada and Great Valley are consistent with far field right-lateral shear strain caused by the San Andreas fault system (Figure 4). Data from sites as far east as Quincy are used in the dislocation models and are well fit by those models. We observe no significant deformation within the Great Valley or Sierra Nevada west of Quincy that is not related to the known faults of the San Andreas fault system. Thus the North America–Pacific plate boundary in northern California is partitioned into a strike-slip portion, the San Andreas fault system, and an extensional portion, the Basin and Range, with a stable block lying between them. Ideally, we could use the data from this network to better constrain the Sierra Nevada–Pacific relative motion, but since these data come from only a narrow strip across the Great Valley and Sierra Nevada, they are not sufficient to add significant constraints on SNGV motion. Data from sites in the southern Sierras must be combined with this data set to estimate the motion of the SNGV block.

None of the sites east of Quincy show velocities significantly different from zero relative to Quincy. Uncertainties for these sites are significantly larger than for the sites in the Coast Ranges because we acquired less data for these sites. It appears that most or all of the shear associated with the northern extension of the ECSZ must lie to the east of this network, although a few millimeters per year could be allowed within the network given the uncertainties. There is no evidence for any significant deformation associated with the lineament of microseismicity between Lake Tahoe and Mount Shasta noted by *Hill et al.* [1990].

6. Conclusions

We used motions of 54 sites in an east-west transect across California at 38°-40° north estimated from GPS observations over a 4-year span to study tectonic problems in the plate boundary zone in northern California. Relative to any well-determined site in the network, velocities of the best determined sites are 1-3 mm/yr in the horizontal components and 3-5 mm/yr in the vertical. We model the velocities in a Pacific plate-fixed frame. Because none of the sites in this network are unambiguously on the stable interior of the Pacific plate, the uncertainty in the motion of the entire network relative to the Pacific plate is larger than the uncertainty in relative motions for many of the sites. Several sites are located on the Sierra Nevada–Great Valley block, but the motion of this block relative to the Pacific and North American plates is too poorly constrained for it to be a more effective reference for the velocities.

The GPS velocities from this network place tight constraints on the total slip rate on all faults of the San Andreas fault system, which we estimate to be $39.6^{+1.5}_{-0.6}$ mm/yr (68.6% confidence). Slip rates on the individual faults are determined less precisely due to inherent tradeoffs between slip rate and locking depth, and between slip rates on adjacent faults. Our best fitting model fits the fault-parallel velocities with a mean square error of 1.04, with the following estimated slip rates (all in millimeters per year with 68.6% confidence intervals): San Andreas fault, $17.4^{+2.5}_{-3.1}$ mm/yr; Ma'acama fault, $13.9^{+4.1}_{-2.8}$ mm/yr; Bartlett Springs fault $8.2^{+2.1}_{-1.9}$ mm/yr. The data are fit best by models in which the San Andreas fault is locked to 15 km, the Ma'acama fault locked to 13 km except for shallow creep in the upper 5 km, and the Bartlett Springs fault creeping at all depths. Locking depths in general are not as well constrained as slip rates. Our estimated slip rate on the San Andreas fault is lower than all geological estimates, although the 95% confidence interval overlaps the range of geologic estimates. Our estimate of the Ma'acama fault slip rate is greater than slip rate estimates for the Hayward or Rodgers Creek faults, its continuation to the south. The Ma'acama fault most likely poses a significant seismic hazard, as it has a high slip rate and a slip deficit large enough to generate a magnitude 7 earthquake today, since there have been no significant earthquakes on the fault in recorded history. The shallow creep observed on the Ma'acama fault relieves only a fraction of the tectonic stress.

We find little or no geodetic evidence for contraction across Coast Ranges, except possibly at western edge of Great Valley where 1-3 mm/yr of shortening is permitted by the data. This amount of contraction would also make the local strike of the Ma'acama fault agree with the direction of relative plate motion throughout the network. More data and three-dimensional models are required to constrain shortening rates across the Coast Ranges.

No strain is observed within the Great Valley or Sierra Nevada except that associated with right-lateral strike slip on the San Andreas fault system. This is consistent with models of the Pacific–North America plate boundary zone in which the relative plate motion is partitioned into two domains, one strike-slip and one dominantly extensional, separated by the elastically deforming Sierra Nevada-Great Valley block. No displacements are associated with the Truckee-Shasta seismic lineation, suggesting that if the Truckee-Shasta lineation defines a tectonic feature its slip rate is very low. Similarly, no right-lateral strain is observed on a possible northern extension of the Eastern California Shear Zone, nor is any appreciable extension across the Honey Lake Fault, the westernmost extensional fault clearly associated with the Basin and Range at this latitude.

The azimuths of site velocities relative to the Pacific plate change systematically with latitude, as do the strikes of faults within the Coast Ranges. The magnitude of the change in azimuth, 15°-20°, is about the same for the GPS velocities, fault strikes, and relative plate motion. The strong correlation between average fault strike and plate motion suggests that the fault strikes in the Coast Ranges may be controlled by the deep flow pattern caused by relative plate motions. A change of several degrees in the direction of relative plate motion over an area only 200 km wide is unusual and requires rotational tectonics not found in the rest of the San Andreas fault system in northern California. However, any interpretation of the changes in fault strike is hampered by uncertainty in the estimated Sierra Nevada block's motion relative to either the Pacific or North American plates.

7. Future Work

Future work should focus on four main areas: more field observations to yield more precise velocities in certain areas, a better realization of the Pacific plate reference frame, a better determination of the SNGV block motion in a plate framework,

and integration of this network with others in northern California to allow systematic inversions for fault slip rates from the San Francisco Bay to Cape Mendocino. More precise velocities are required in the Sierra Nevada, where site velocities are only determined with a precision of several millimeters per year. Some data collected after 1995 will address this need. More precise velocities, especially in the east component, are needed in the Coast Ranges and at the western edge of the Great Valley to better constrain the rate of convergence normal to the San Andreas system. Data from new sites between the Ma'acama and Bartlett Springs fault, especially on the southern Ukiah profile, would be useful in reducing some of the trade-offs between the slip rates on those two faults. A systematic integration of geodetic data spanning all of northern California and inversion of this data for fault slip rates throughout the area will allow for a rigorous comparison of geodetic fault slip rates at several places along the strike of the SAF system.

A better realization of Pacific plate reference frame would have several benefits. First, it would improve the estimation of the SAF and other slip rates by reducing the ambiguity evident in the difference between the optimal model and alternate model, which differ only in the assumed precision of the definition of the Pacific plate reference frame. Second, it would aid in the interpretation of the azimuth changes of the GPS velocities and their relationship to local fault slip rates. Better realization of a Pacific plate frame would require expanding the velocity solution to include the entire North American and Pacific plates, as well as resolving difference in the North America–Pacific relative plate motion as measured by NUVEL-1A and space geodesy [e.g., *Larson et al.*, 1997].

A better determination of the motion of the SNGV relative to the Pacific and North American plates is required to constrain the expected rates of SAF-normal contraction. The differences between existing models for SNGV block motion are small, but significant compared to the rate of fault-normal shortening. With geodetic networks having a horizontal velocity precision of ~1 mm/yr becoming common throughout northern California, and with efforts being mounted to account for fault slip rates at the mm/yr level, the motion of the SNGV relative to the Pacific and North American plates needs to be given closer attention, as a better understanding of the plate motions actually accommodated on the San Andreas fault system is required to further advance knowledge about the fault system. Data from the southern Sierra Nevada must be combined with data from the north to give the best determination of the block motion.

Acknowledgments. The GIPSY/OASIS II software was developed at the Jet Propulsion Laboratory of the California Institute of Technology. We thank Greg Beroza, Susan Owen, Doug Dodge, Wendy Wempe Corona, Tony Mossop, and many others for working in the field. Yehuda Bock (Scripps Institute of Oceanography) helped in locating the data and field information for the 1991 HPGN survey. We gratefully acknowledge the organizations that operate permanent GPS sites and make the data freely available through the IGS or other means. In particular, the Penticton site is operated by the Geological Survey of Canada, and the Quincy site is operated by JPL with NASA support. This work would not have been so successful without the assistance of many data archivists who helped us find old global network data: Keith Stark (Scripps, JPL), Dave Starr (JPL), Carey Noll (CDDIS), Stephen Delahunt (Geodetic Survey of Canada). Figures were generated using Generic Mapping Tools (GMT) version 3 [*Wessel and Smith*, 1995]. We thank Roland Bürgmann, Ken Hurst, an anonymous reviewer, and the Associate Editor for helpful comments and reviews. This research was supported by National Science Foundation grant EAR-9116117 to Stanford University.

References

Argus, D. and R. G. Gordon, Current Sierra Nevada – North America motion from Very Long baseline Interferometry: Implications for the kinematics of the western United States, *Geology, 19*, 1085-1089, 1991.

Arnadóttir, T., and P. Segall, The 1989 Loma Prieta earthquake imaged from inversion of geodetic data, *J. Geophys. Res., 99*, 21,835–21,855, 1994.

Berg, B. A., Locating global minima in optimization problems by a random-cost approach, *Nature, 361*, 708–710, 1993.

Boucher, C., Z. Altamimi, M. Feissel, and P. Sillard, Results and analysis of the ITRF 94, *IERS Tech. Note 20*, IERS Cent. Bur., Obs. De Paris, 1996.

Brown, R. D., 1906 surface faulting on the San Andreas fault near Point Delgada, California, *Bull. Seismol. Soc. Am.*, 85, 100-110, 1995.

Budding, K. E., D. P. Schwartz, and D. L. Ostergren, The Rodgers Creek fault zone, CA: Slip rate and recurrence estimates, *Seismol. Res. Lett., 62*, 12, 1991.

Castillo, D. A., and W. L. Ellsworth, Seismotectonics of the San Andreas fault system between Point Arena and Cape Mendocino in Northern California; implications for the development and evolution of a young transform, *J. Geophys. Res., 98*, 6543-6560, 1993.

Cervelli, P., M. H. Murray, and P. Segall, Imaging deformation sources with geodetic data, (abstract), *EOS Trans. AGU, 79(45), Fall Meeting Suppl.*, F33, 1998.

Cline, M. W., R. A. Snay, and E. L. Timmerman, Geodetically derived strain from San Francisco Bay to the Mendocino triple junction, California, *NOAA Tech. Rep. NGS 311*, 17 pp., Nat. Oceanic and Atmos. Admin., Silver Spring, Md., 1985.

Curray, J. R., and R. D. Nason, San Andreas fault north of Point Arena, CA, *Geol. Soc. Am. Bull., 78*, 413-418, 1967.

DeMets, C., R. Gordon, D. Argus, and S. Stein, Current plate motions, *Geophys. J. Int., 101*, 425-478, 1990.

DeMets, C., R. G. Gordon, D. F. Argus, and S. Stein, Effects of recent revisions to the geomagnetic reversal time scale on estimates of current plate motions, *Geophys. Res. Lett., 21*, 2191-2194, 1994.

Dixon, T. H., S. Robaudo, and J. Lee, Constraints on present-day Basin and Range deformation from Space Geodesy, *Tectonics, 14*, 755-772, 1995.

Efron, B., and R. Tibshirani, Bootstrap methods for standard errors, confidence intervals, and other measures of statistical accuracy, *Stat. Sci., 1*, 54–77, 1986.

Elósegui, P., J. L. Davis, R. T. K. Jaldehag, J. M. Johansson, A. E. Niell, and I. I. Shapiro, Geodesy using the Global Positioning System: The effects of signal scattering on estimates of site position, *J. Geophys. Res., 100*, 9921-9934, 1995.

Fares, N., and J. R. Rice, Crustal deformation modeling for San Andreas fault earthquake cycles, *EOS Trans. AGU, 70*, 603, 1989.

Frizell, V. A. Jr. and R. D. Brown Jr., Map showing recently active breaks along the Green Valley fault, Napa and Sonoma Counties, California, *US Geol. Surv. Misc. Field Stud. Map MF-743*, scale 1:24,000, 1976.

Furlong, K. P., W. D. Hugo, and G. Zandt, Geometry and evolution of the San Andreas fault zone in northern California, *J. Geophys. Res., 94*, 3100-3110, 1989.

Furlong, K. P., Thermal-rheologic evolution of the upper mantle and the development of the San Andreas fault system, *Tectonophysics, 223*, 149-164, 1993.

Galehouse, J. S., Theodolite measurements of creep rates on San Francisco Bay region faults, in *National Earthquake Hazards Reduction Program, Summaries of Technical Reports*, vol. XXXV, compiled by M. Jacobson, *U.S. Geol. Surv. Open File Rep., 84-176*, 328-338, 1994.

Gilbert, L. E., C. H. Scholz, and J. Beavan, Strain localization along the San Andreas fault: Consequences for loading mechanisms, *J. Geophys. Res., 99*, 23,975-23,984, 1994.

Gordon, D., C. Ma, and J. W. Ryan, Results from the CDP mobile VLBI program in the western United States, in *Contributions of Space Geodesy to Geodynamics: Crustal Dynamics*, edited by D. E. Smith and D. L. Turcotte, *Geodyn. Ser.*, vol. 23, AGU, Washington, D. C., pp. 131-138, 1993.

Gregorius, T., GIPSY-OASIS II: A User's Guide, (self-published), Univ. of Newcastle, Newcastle, England, U.K., 1996.

Heflin, M., et al., Global Geodesy using GPS without fiducial sites, *Geophys. Res. Lett., 19*, 131-134, 1992.

Hill, D. P., J. P. Eaton, and L. M. Jones, Seismicity, 1980-86, in *The San Andreas Fault System, California*, edited by Robert E. Wallace, *U.S. Geol. Surv. Prof. Pap., 1515*, 115-151, 1990.

Hole, J. A., B. C. Beaudoin, and T. J. Henstock, Wide-angle seismic constraints on the evolution of the deep San Andreas plate boundary by Mendocino triple junction migration, *Tectonics*, *17*, 802-818, 1998.

Jachens, R. C., and A. Griscom, Three-dimensional geometry of the Gorda plate beneath northern California, *J. Geophys. Res.*, *88*, 9375-9392, 1983.

Johnson, H. O., and F. K. Wyatt, Geodetic network design for fault-mechanics studies, *manusc. geod.*, *19*, 309-323, 1994.

Kelson, K., W. R. Lettis, and M. Lisowski, Distribution of geologic slip and creep along faults in the San Francisco bay region, in *Proceedings of the Second Conference on Earthquake Hazards in the Eastern San Francisco Bay Area*, edited by G. Borchardt, et al., *Spec. Publ. 113*, Calif. Dep. of Conserv., Div. of Mines and Geol., 31-38, Sacramento, 1992.

Larson, K. M., J. T. Freymueller, and S. Philipsen, Global plate velocities from the Global Positioning System, *J. Geophys. Res.*, *102*, 9961-9981, 1997.

Lawson, A. C., The California earthquake of April 18, 1906: Report of the State Earthquake Investigation Commission, 3 vols., *Carnegie Inst. Washington Publ.*, *87*, 1 atlas, 1908.

Li, V. C., and J. C. Rice, Crustal deformation in great California earthquake cycles, *J. Geophys. Res.*, *92*, 11,533-11,551, 1987.

Lienkaemper, J. J., G. Borchardt, and M. Lisowski, Historic creep rate and potential for seismic slip along the Hayward fault, California, *J. Geophys. Res.*, *96*, 18,261-18,283, 1994.

Lisowski, M., J. C. Savage and W. H. Prescott, The velocity field along the San Andreas fault in central and southern California. *J. Geophys. Res.*, *96*, 8369-8389, 1991.

Ma, C., et al., Goddard Space Flight Center VLBI annual report, Goddard Space Flight Cent., Greenbelt, Md., 1995.

Matthews, M. V., and P. Segall, Statistical inversion of crustal deformation data and estimation of the depth distribution of slip in the 1906 earthquake, *J. Geophys. Res.*, *98*, 12,153--12,163, 1993.

McLaughlin, R. J., D. H. Sorg, J. L. Morton, T. G. Theodore, C. E. Meyer, and M. H. Delevaux, Paragenesis and tectonic significance of base and precious metal occurrences along the San Andreas fault at Point Delgada, California, *Econ. Geol.*, *80*, 344-359. 1985.

McLaughlin, R. J., W. V. Sliter, N. O. Frederikson, W. P. Harbert, and D. S. McCulloch, Plate motions recorded in tectonostratigraphic terranes of the Franciscan complex and evolution of the Mendocino triple junction, northwestern California, *U.S. Geol. Surv. Bull.*, *1997*, 60 pp., 1994.

Merritts, D. J., The Mendocino triple junction: Active faults, episodic coastal emergence, and rapid uplift, *J. Geophys. Res.*, *101*, 6051-6070, 1996.

Minster, J. B., and T. H. Jordan, Vector constraints on western U.S. deformation from space geodesy, neotectonics, and plate motions, *J. Geophys. Res.*, *92*, 4798-4808, 1987.

Murray, M. H., G. A. Marshall, M. Lisowski, and R. S. Stein, The 1992 *M*=7 Cape Mendocino, California, earthquake: Coseismic deformation at the south end of the Cascadia megathrust, *J. Geophys. Res.*, *101*, 17,707–17,725, 1996.

Niemi, T. M., and N. T. Hall, Late Holocene slip rate and recurrence of great earthquakes on the San Andreas fault in northern California, *Geology*, *20*, 195-198, 1992.

Oppenheimer, D., et al., The Cape Mendocino, California, earthquakes of April 1992: Subduction at the triple junction, *Science*, *261*, 433-438, 1993.

Pezzopane, S. K., and R. J. Weldon, Tectonic role of active faulting in central Oregon, *Tectonics*, *12*, 1140-1169, 1993.

Prentice, C. S., Earthquake geology of the northern San Andreas fault near Point Arena, California, Ph.D. thesis, 349 pp., Calif. Inst. of Technol., Pasadena, 1989.

Prescott, W. H., and S. B. Yu, Geodetic measurement of horizontal deformation in the northern San Francisco bay region, California, *J. Geophys. Res.*, *91*, 7475-7484, 1986.

Savage, J. C., and R. O. Burford, Geodetic determination of relative plate motion in California, *J. Geophys. Res.*, *78*, 832-845, 1973.

Savage, J. C., and M. Lisowski, Inferred depth of creep on the Hayward fault, central California, *J. Geophys. Res.*, *98*, 787-793, 1993.

Savage, J. C., M. Lisowski, and W. H. Prescott, An apparent shear zone trending north-northwest across the Mojave Desert into Owens Valley, eastern California, *Geophys. Res. Lett.*, *17*, 2113-2116, 1990.

Schwarz, D. P., D. Pantosti, S. Hecker, K. Okumura, K. E. Budding, and T. Powers, Late Holocene behavior and seismogenic potential of the Rodgers Creek fault zone, Sonoma County, California, in *Proceedings of the Second Conference on Earthquake Hazards in the Eastern San Francisco Bay Area*, edited by G. Borchardt, et al., *Spec. Publ. 113*, Calif. Dep. of Conserv., Div. of Mines and Geol., 393-398, Sacramento, 1992.

Sibson, R. H., Fault zone models, heat flow, and the depth distribution of earthquakes in the continental crust of the United States, *Bull. Seismol. Soc. Am.*, *72*, 151-163, 1982.

Sibson, R. H., Continental fault structure and the shallow earthquake source, *J. Geol. Soc. London*, *140*, 741-767, 1983.

Thatcher, W., Strain accumulation and release mechanism of the 1906 San Francisco earthquake, *J. Geophys. Res.*, *80*, 4862-4872, 1975.

Thatcher, W., G. Marshall, and M. Lisowski, Resolution of fault slip along the 470 km long rupture of the great 1906 earthquake and its implications, *J. Geophys. Res.*, *102*, 5353-5367, 1997.

Unruh, J. R., B. A. Loewen, and L. R. Munk, Seismic hazard assessment of an active blind thrust beneath the Rumsey Hills, southwestern Sacramento Valley, California, *Eos Trans. AGU*, *73*, 589-590, 1992.

Ward, S. N., Pacific–North America plate motions: New results from Very Long Baseline Interferometry, *J. Geophys. Res.*, *95*, 21,965-21,981, 1990.

Wessel, P., and W. H. F. Smith, New version of the Generic Mapping Tools released, *Eos Trans. AGU*, *76*, 329, 1995.

Williams, S. D. P., J. L. Svarc, M. Lisowski, and W. H. Prescott, GPS measured rates of deformation in the northern San Francisco Bay region, California, 1990-1993, *Geophys. Res. Lett.*, *21*, 1511-1514, 1994.

Wise, D. U., An outrageous hypothesis for the tectonic pattern of the North American cordillera, *Geol. Soc. Am. Bull.*, *74*, 357-362, 1963.

Working Group on Northern California Earthquake Potential, Database of potential sources for earthquakes larger than magnitude 6 in Northern California, *U.S. Geol. Surv. Open File Rep.*, *96-705*, 1996.

Wright, L., Late Cenozoic fault patterns and stress fields in the Great Basin and eastward displacement of the Sierra Nevada block, *Geology*, *4*, 489-494, 1976.

Zumberge, J. F., M. B. Heflin, D. C. Jefferson, M. M. Watkins, and F. H. Webb, Precise point positioning for the efficient and robust analysis of GPS data from large networks, *J. Geophys. Res.*, *102*, 5005-5018, 1997.

D. C. Castillo, Department of Geology and Geophysics, University of Adelaide, Adelaide, Australia.

J. T. Freymueller, Geophysical Institute, University of Alaska, Fairbanks, AK 99885. (jeff@giseis.alaska.edu)

M. H. Murray and P. Segall, Department of Geophysics, Stanford University, Stanford, CA 94305. (mmurray@pangea.stanford.edu; segall@pangea.stanford.edu)

(Received June 4, 1998; revised December 11, 1998;
accepted December 16, 1998.)